02

Advanced Optical Metrology

Thin Film Metrology

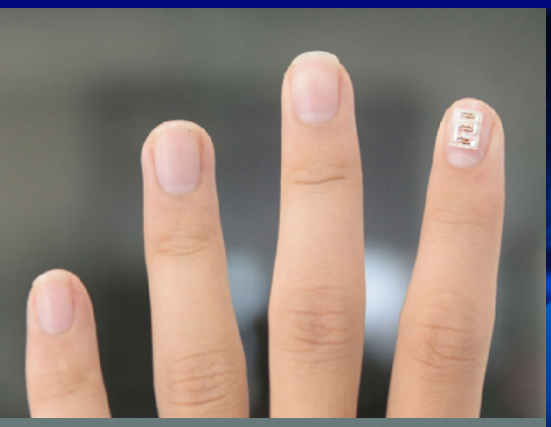

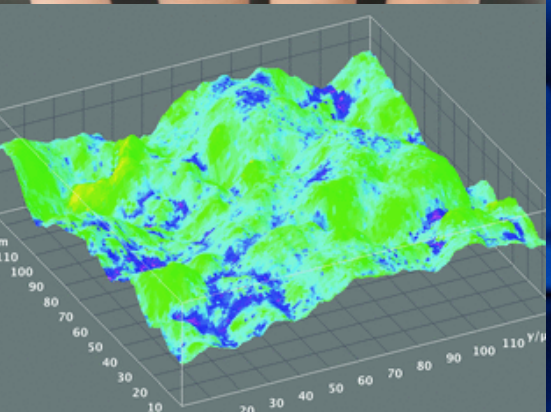

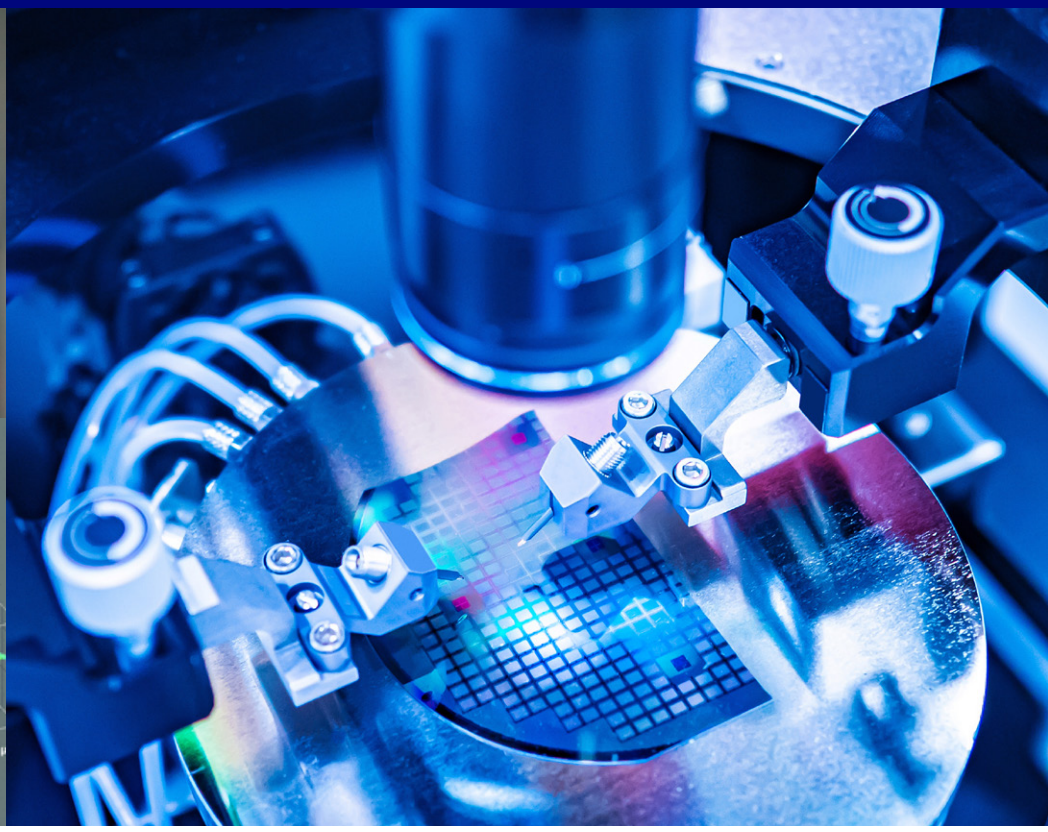

OLYMPUS

WILEY

Contents

Imprint

© Wiley-VCH Verlag GmbH & Co. KGaA
Boschstr. 12, 69469 Weinheim, Germany
Email: info@wiley-vch.de
Editor-in-Chief: Dr. Christina Poggel
Editor: Dr. Lawrence Renna

Thin Film Metrology

Thin film technology is ubiquitous across materials science for applications such as semiconductors,[1,2] electronics (*e.g.*, light-emitting diodes, soft electronics),[2,3] microelectromechanical systems (MEMS),[4] memory devices,[2,5] energy storage (batteries, capacitors),[6,7] photovoltaics,[8,9] fuel generation,[10] catalysis,[11] chemical sensors,[12,13] environmental coatings (*e.g.*, thermal),[14] chemical barriers (*e.g.*, diffusion, corrosion),[15,16] radiation detection,[2] photodetectors,[17] microfluidics,[18] piezoelectric devices,[19] mechanical layers (*e.g.*, adhesion, lubrication, hardness),[20–22] magnetic devices (*e.g.*, SQUID),[23] optical coatings (*e.g.*, electrochromic, antireflection, interference, waveguides),[24] biomaterials and biomedical applications,[25] and many more. Furthermore, there are sufficient fabrication techniques that virtually any type of material can be prepared as a thin film, such as metals, alloys, oxides, ceramics, glasses, polymers, inorganic complexes, organic molecules, and biological molecules.

The ability to prepare a material into a thin film can enable specific material properties and unlock particular applications. Often, the nano-, micro-, and millimeter-scale morphologies of the thin film have important implications on its properties and eventual application. Therefore, the characterization of the morphology of thin films is an integral part of materials science research. There are a variety of different characterization techniques with different pros and cons in terms of resolution, the field of view, sample size, ease of use, speed, and information that can be obtained.

This brief introduction will discuss some of the techniques to characterize thin films. The methods are characterized by their distinct operating principles, namely mechanical characterization techniques, thermal analyses, scanning probe methods, and methods that involve the interaction of radiation (*e.g.*, electrons, ions, and photons) with matter. The introduction will highlight laser scanning confocal microscopy as a promising method to characterize the morphology of a wide variety of thin-film materials.

THIN FILM CHARACTERIZATION

Mechanical Characterization. The mechanical properties of a thin film can provide information on the underlying morphology of the material. The manner in which a thin film responds to a particular mechanical deformation is dependent on the assembly of its constituent components. Furthermore, the influence of volumetric and interfacial constraints can cause mechanical properties to differ from bulk values. Cantilever beam or plate type structures are commonly used to measure residual stress, from deflection and curvature measurements. The Young's modulus and plastic properties of thin films can be determined by analyzing the stress associated with thermal cycling using thin wafer or cantilever beam measurements. Elastic moduli and other mechanical properties of thin films can be measured by cantilever beam resonant frequency methods. Furthermore, measurement techniques such as microindentation and substrate curvature can be utilized to determine the plastic properties of submicron thin films and multilayers on substrates. Peel, pull, and scratch tests are used to characterize the adhesion properties of materials; however, they do not provide quantitative information regarding interfacial atomic bonding strength. Lastly, microindentation and micro-scratch characterization methods can provide a further understanding of the mechanical processes of thin films.[26]

Thermal Characterization. The thermal properties of materials can also shed light on the underlying morphology of thin films. Thermal characterization can provide physical and chemical information of the thin film.[27] Thermogravimetric analysis (TGA) is used to measure the mass change of a sample as a function of temperature. The off-gas from TGA experiments can be analyzed by mass spectrometry (MS) and Fourier transform infrared spectroscopy (FTIR) to understand the chemistry of the thermal decomposition products.[28] Differential thermal analysis (DTA) measures the temperature differences between a sample and a reference as they are simultaneously heated or cooled, whereas differential scanning calorimetry (DSC) measures the difference in heat flow. Both DTA and DSC can be used to determine properties such as the crystallinity, glass transition, phase changes, chemical reactions, heat capacity, etc.[27,29] Finally, dynamic infrared thermography can be used to determine the thermal conductivity, heat capacity, and thermal diffusivity of thin films.[30]

Scanning Probe Characterization. Physical probes can be used to scan the surface of thin films to understand both their surface and, to some extent, their bulk morphologies. Surface profilometry is a useful tool for measuring the thickness, roughness, and texture of thin films. In profilometry, a stylus probe is brought into direct contact with the film, and a line scan is performed.[31] In atomic force microscopy (AFM), a sharp probe is raster-scanned across a sample surface, in contact or non-contact modes. Interaction forces between the sample and the probe are measured by the deflection of the cantilever containing the probe and used to generate an image.[32] Different force modes can be analyzed, such as attractive, repulsive, magnetic, electrostatic, and van der Waals. In certain thin conductive films, bulk morphologies can be constructed using conductive AFM (cAFM).[33] Also, Kelvin probe force microscopy (KPFM) can be used to measure charge accumulation[34] and the work function of thin films.[35] Although AFM is capable of sub-nm resolution and is nondestructive, it is not rapid, it is susceptible to artifacts, and has difficulties capturing large variations in sample thickness.[36] Scanning electrochemical microscopy (SECM) uses an ultramicroelectrode tip and can be used to map the electrochemical activity of a thin film.[37] Finally, scanning tunneling microscopy (STM) utilizes a metallic probe which is scanned over a thin film, and a voltage is applied between the tip and the surface. In this way, the quantum tunneling current is used to image the sample.[38] STM can achieve angstrom-scale resolution but requires specialized vacuum equipment.

Electron Microscopy. Transmission electron microscopy (TEM) can be used to elucidate the structure, chemistry, and properties of thin films. In TEM, the transmission of an electron beam through a sample is used to generate an image. Since electrons interact strongly with matter, both structural and chemical information can come from TEM characterization. Additional techniques in TEM include selected area electron diffraction (SAED), electron energy loss spectroscopy (EELS), and energy-filtered TEM (EFTEM). In TEM, due to the small de Broglie wavelength of electrons, the lattice spacing of atoms can be imaged. The sample requires special preparation and must be very thin so that the electron beam is not attenuated by the sample, and special vacuum equipment is required.[39] Meanwhile,

in scanning electron microscopy (SEM), an electron beam is raster-scanned over a sample, and either secondary electrons or backscattered electrons from the sample are detected to map the sample topology. SEM has a wider field of view than TEM, and it does not require ultrathin samples because it does not rely on electrons being transmitted through the sample; however, the resolution of SEM is less than TEM, around 1 nm. Further, energy-dispersive X-ray spectroscopy (EDS) can be used to spatially map the elemental content of thin films. Also, the orientation and phase of crystalline domains can be determined by the diffraction of backscattered electrons (EBSD).[40]

Ion Beam Techniques. Helium ion microscopy (HeIM) is an imaging technique similar to SEM, but instead of an electron beam, a helium ion beam is scanned over the sample. Secondary electrons ejected from the sample due to the impact of helium ions are detected. The HeIM beam can be less than 1 nm, enabling high resolution with a fairly wide field of view.[41] In another method, elemental maps of thin films can be constructed by time-of-flight secondary ion mass spectrometry, where a pulsed ion beam is scanned over a sample, which removes particles from the surface that are detected by MS.[42]

X-ray-based Techniques. The interaction of X-rays (and neutrons, which is not discussed here) with matter is a useful tool to determine thin film morphology. Small-angle X-ray scattering (SAXS) characterization of a thin film, either in transmission or grazing incidence (*i.e.*, GISAXS) configurations,[43] can give information on the periodic structures in the film at the nanometer scale. Whereas, X-ray diffraction (XRD) and wide-angle X-ray scattering can provide structural information at the angstrom-scale.[44] Soft/resonant X-rays can be used to probe particular chemical groups in the material.[45] Furthermore, X-ray reflectivity (XRR) is a useful tool for determining the thickness of thin films.[46] Lastly, X-ray microtomography (μCT) uses X-rays to create cross-sections of samples, which can be constructed into 3D images.[47]

Photon-based Methods. Optical microscopy (OM) is one of the oldest methods to determine a sample's morphology, dating back to the seventeenth century. OM is one of the most important techniques for identifying features > 500 nm in materials and thin films. Par-

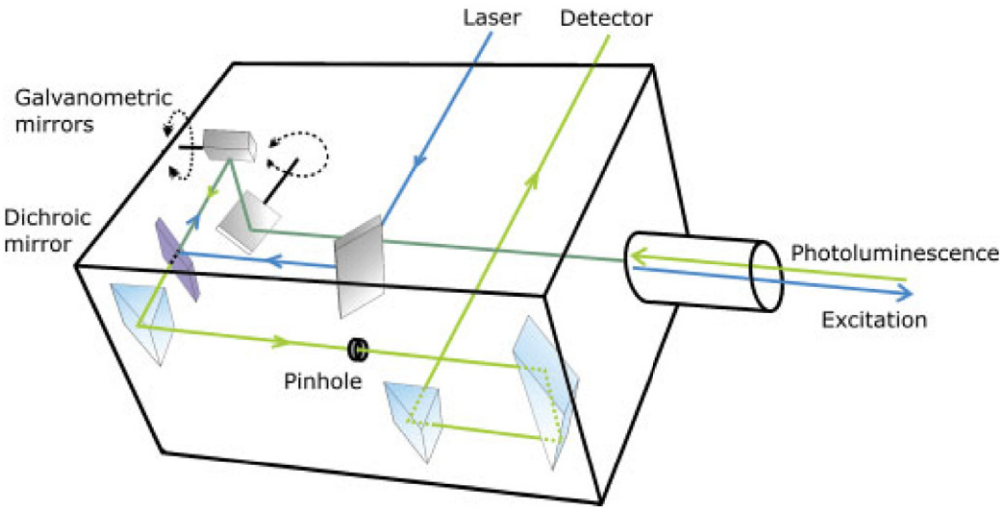

Figure 1: Schematic of the laser scanning head of the LSCM. The incoming laser beam is reflected by the dichroic mirror and directed toward the sample by the two galvanometric mirrors. The reflected, transmitted, or fluoresced light from the sample is transmitted by the dichroic mirror and is spatially filtered by the pinhole before reaching the detector.

ticular techniques in OM include brightfield, darkfield, polarization, interference, and phase-contrast microscopies. Contrast in OM is created by various mechanisms, depending on the imaging mode, such as absorption of light, scattering, rotation of polarized light, and interference.[48] Lastly, near-field scanning optical microscopy (NSOM) is a technique where nanoscale morphologies can be elucidated by scanning a small fiber-optic probe over thin films. When the distance between the probe and the sample is smaller than the wavelength of light, the resolution of the image is not limited by the optical wavelength.[49] Finally, confocal microscopy has several advantages over conventional widefield OM, such as the ability to control depth of field, elimination or reduction of background information, and the capability to collect serial optical sections from specimens.[36,48,50] In particular, laser confocal scanning microscopy will be discussed in the next section.

LASER CONFOCAL SCANNING MICROSCOPY

In far-field optical techniques, imaging is accomplished by focusing elements. In a microscope, the objective lens forms a magnified image of the illuminated object that can then be examined with the eyepiece. If we consider the image of a single point, the light intensity is distributed around the focal point in a focal volume described by a point spread function (PSF). The extent of the PSF determines the resolution. In the ideal case where no aberrations are present, the resolution is limited by diffraction and is determined by the wavelength of light in the medium (λn) and the aperture angle of the lens $NA=n\sin(\upsilon)$, where n is the refractive index of the medium and υ is the half-angle of the lens aperture, and can be expressed by the Rayleigh theoretical resolution limit : $RL=0.61\lambda/NA$. Much research has been devoted to developing tools able to image objects with a resolution lower than the Rayleigh limit. By confocal microscopy, a resolution about 30% less than the Rayleigh limit is obtained. This considerable advantage of confocal microscopy follows by the use of a point detector, obtained in practice by placing a circular pinhole in front of the photodetector that cuts off the out-of-focus light from surrounding planes.[36]

Although the confocal microscope was invented in 1955 by Minsky,[51] it was not widely adopted until the invention of lasers and the availability of high-performance computing. Laser scanning confocal microscopes (LSCMs) use collimated laser light as a 'point' illumination source, with point focus on the sample, and focus the reflected, transmitted, or fluoresced light through a pinhole to provide a 'point' detector. A schematic of the laser scanning head is shown in Figure 1. [50]

Multiple imaging detection modes can be used with LSCM, including but not limited to

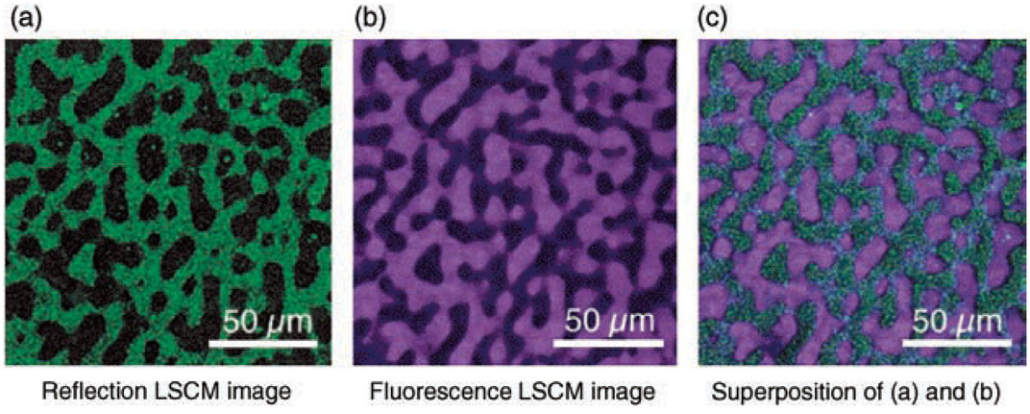

Figure 2: LSCM images of poly(styrene-ran-butadiene) and polybutadiene films, using (a) reflection and (b) fluorescence modes. (c) Superposition of reflection LSCM and fluorescence LSCM images.

reflected light, transmitted light, fluorescence, and Raman spectroscopy. The different imaging modes can provide different information about the thin film, and the different modes can be superimposed to create a composite image of the sample (Figure 2).[48] As long as surface topology is the only characterization needed, reflection mode can be an ideal method to characterize thin films.[52] One benefit of reflection mode for materials science is that the material does not need to be fluorescent to be imaged; this is ideal for many materials systems. Thus, as-prepared samples can easily be characterized. For reflected light imaging, the smallest available wavelength laser (*e.g.*, 405 nm) is optimal, as the optical resolution is directly proportional to wavelength.[50] The high spatial resolution, wide field of view, minimal sample preparation, relative ease of measurement (*i.e.*, no vacuum equipment required), the ability to characterize samples that have large height variation, the ability to construct 3D and pseudo-infinite depth of field imaging, and versatility (*i.e.*, material selection and imaging modes) of LSCM make it an ideal tool of characterizing the morphology of thin films in materials science.

REFERENCES

[1] *E. Fortunato, P. Barquinha, R. Martins, Adv. Mater. 2012, 24, 2945.*

[2] *Z. Wang, P. K. Nayak, J. A. Caraveo-Frescas, H. N. Alshareef, Adv. Mater. 2016, 28, 3831.*

[3] *M. Kim, C. Kim, H. Alrowais, O. Brand, Adv. Mater. Technol. 2018, 3, 1800061.*

[4] *S. Trolier-McKinstry, P. Muralt, J. Electroceramics 2004, 12, 7.*

[5] *D. B. Strukov, G. S. Snider, D. R. Stewart, S. R. Williams, Nature 2008, 453, 80.*

[6] *S. Moitzheim, B. Put, P. Vereecken, Adv. Mater. Interfaces 2019, 6, 1900805.*

[7] *M. Yu, X. Feng, Joule 2019, 3, 338.*

[8] *B. Kippelen, J.-L. Brédas, Energy Environ. Sci. 2009, 2, 251.*

[9] *S. Sundaram, K. Shanks, H. Upadhyaya, "Thin Film Photovoltaics" in A Comprehensive Guide to Solar Energy Systems 2018, 361.*

[10] *R. Shwetharani, H. R. Chandan, M. Sakar, G. Balakrishna, K. Reddy, A. Raghu, Int. J. Hydrog. Energy 2019.*

[11] *C. Guizard, A. Princivalle, Catal. Today 2009, 146, 367.*

[12] *H. Mukamal, S. Cordero, D. Ruiz, M. Beshay, R. Lieberman, Proc. SPIE 2005, 6004, 600406.*

[13] *C. Mackin, A. Fasoli, M. Xue, Y. Lin, A. Adebiyi, L. Bozano, T. Palacios, 2D Mater. 2020, 7, 022002.*

[14] *J. Thakare, C. Pandey, M. Mahapatra, R. Mulik, Met. Mater. Int. 2020, 1.*

[15] *L. H. Hihara, "Electrochemical aspects of corrosion-control coatings" in Intelligent Coatings for Corrosion Control 2015, 1.*

[16] *L. Körner, A. Sonnenfeld, P. Rohr, Plasma Process. Polym. 2009, 6, S660.*

[17] *Z. Han, H. Liang, W. Huo, X. Zhu, X. Du, Z. Mei, Adv. Opt. Mater. 2020, 8, 1901833.*

[18] *M. Focke, D. Kosse, C. Müller, H. Reinecke, R. Zengerle, F. Stetten, Lab Chip 2010, 10, 1365.*

[19] *A. Khan, Z. Abas, H. Kim, I.-K. Oh, Smart Mater. Struct. 2016, 25, 053002.*

[20] *S. Mishra, D. Verma, S. Bysakh, L. Pathak, J. Nanomater. 2013, 2013, 1.*

[21] *S. Lučić, V. Kovačević, D. Hace, Int. J. Adhes. Adhes. 1998, 18, 115.*

[22] *E. W. Roberts, Tribol. Int. 1990, 23, 95.*

[23] *G. Ehnholm, T. Wiik, T. Stubb, Jpn. J. Appl. Phys. 1977, 16, 261.*

[24] *A. Piegari, F. Flory, Optical thin films and coatings: From materials to applications; 2018.*

[25] *H. Griesser, Thin film coatings for biomaterials and biomedical applications; 2016.*

[26] *P. S. Alexopoulos, T. C. O'Sullivan, Annu. Rev. Mater. Sci. 1990, 391.*

[27] *A. W. Coats, J. P. Redfern, Analyst 1963, 88, 906.*

[28] *L. Renna, F.-G. Blanc, V. Giordani, J. Electrochem. Soc. 2020, 167, 070542.*

[29] *M. Yu. Efremov, J. T. Warren, E. A. Olson, M. Zhang, A. T. Kwan, L. H. Allen, Macromolecules 2002, 35, 1481.*

[30] *A. Greppmair, N. Galfe, K. Amend, M. Stutzmann, M. Brandt, Rev. Sci. Instrum. 2019, 90, 044903.*

[31] *M. Tosa, "Surface Profilometer" in Compendium of Surface and Interface Analysis 2018, 679.*

[32] *G. Friedbacher, "Atomic Force Microscopy (AFM)" in Surface and Thin Film Analysis: A Compendium of Principles, Instrumentation, and Applications, Second Edition 2011, 443.*

[33] *L. A. Renna, M. Bag, T. S. Gehan, X. Han, P. M. Lahti, D. Maroudas, D. Venkataraman, J. Phys. Chem. B 2016, 120, 2544.*

[34] *L. A. Renna, Y. Liu, T. P. Russell, M. Bag, D. Venkataraman, Mater. Lett. 2018, 217, 308.*

[35] *V. Palermo, M. Palma, P. Samorì, Adv. Mater. 2006, 18, 145.*

[36] *M. A. Loi, E. D. Como, Michele, "Morphology-Correlated Photophysics in Organic Semiconductor Thin Films by Confocal Laser Microscopy and Spectroscopy" in Photophysics of Molecular Materials: From Single Molecules to Single Crystals 2005, 153.*

[37] *G. Lu, J. Cooper, P. McGinn, Electrochim. Acta 2007, 52, 5172.*

[38] *L. Yue, C. Xiangzhen, W. Runwen, Microw. Opt. Technol. Lett. 1989, 2, 135.*

[39] *A. Petford-Long, A. Chiaramonti, Annu. Rev. Mater. Res. 2008, 38, 559.*

[40] *M. Johnson, C. Carter, J. Michael, J. Am. Ceram. Soc. 1999, 82, 1644.*

[41] *A. Pearson, S. Boden, D. Bagnall, D. Lidzey, C. Rodenburg, Nano Lett. 2011, 11, 4275.*

[42] *D. Mao, G. Blatz, C. E. Wickersham, M. Gloeckler, Sol. Energy Mater. Sol. Cells 2016, 157, 65.*

[43] *S. H. Kim, M. J. Misner, T. Xu, M. Kimura, T. P. Russell, Adv. Mater. 2004, 16, 226.*

[44] *A. Hexemer, W. Bras, J. Glossinger, E. Schaible, E. Gann, R. Kirian, A. MacDowell, M. Church, B. Rude, H. Padmore, J. Phys.: Conf. Ser. 2010, 247, 012007.*

[45] *G. M. Su, W. White, L. A. Renna, J. Feng, S. Ardo, C. Wang, ACS Macro Lett. 2019, 8.*

[46] *T. P. Russell, Mater. Sci. Rep. 1990.*

[47] *A. Hierro-Rodriguez, C. Quirós, A. Sorrentino, L. M. Alvarez-Prado, J. I. Martín, J. M. Alameda, S. McVitie, E. Pereiro, M. Vélez, S. Ferrer, arXiv prepr. arXiv 2019, 1907.01261.*

[48] *M. Ramanathan, S. B. Darling, "Optical Microscopy (Polarized, Interference, and Phase-Contrast Microscopy) and Confocal Microscopy" in Characterization of Polymer Blends: Miscibility, Morphology, and Interfaces 2014, 523.*

[49] *P. F. Barbara, D. M. Adams, D. B. O'Connor, Annu. Rev. Mater. Sci 1999, 29, 433.*

[50] *D. B. Hovis, A. H. Heuer, J. Microsc. 2010, 240, 173.*

[51] *M. Minsky, Scanning 1996.*

[52] *A. Ribbe, M. Hayashi, M. Weber, T. Hashimoto, Polymer 1998, 39, 7149.*

01 The Use of Laser Scanning Confocal Microscopy (LSCM) in Materials Science

D.B. Hovis and A.H. Heuer

ABSTRACT

Laser scanning confocal microscopes are essential and ubiquitous tools in the biological, biochemical, and biomedical sciences, and play a similar role to scanning electron microscopes in materials science. However, modern laser scanning confocal microscopes have several advantages for the characterization of materials, in addition to their obvious uses for high resolution reflected and transmitted light optical microscopy. Herein, we provide several examples that exploit the laser scanning confocal microscope's capabilities of pseudo-infinite depth of field imaging, topographic imaging, fluorescence imaging, and photo-stimulated luminescence imaging for the characterization of different materials.

INTRODUCTION

Confocal microscopy is a ubiquitous technique in the life sciences, as it provides precise optical sectioning of fluorescently labeled thick specimens. To date, however, it has been underutilized in materials science. Recent advances in both instrumentation and computing power now make confocal microscopy an attractive imaging and analytical tool for materials scientists. When properly configured, a confocal microscope can serve as a high-resolution optical microscope (in either transmission or reflection) with 'infinite' depth of field, while at the same time serving as a non-contact optical profilometer. Combined and synchronized with an external spectrometer, techniques such as photo-stimulated luminescence spectroscopy are enabled.

Though the confocal microscope was invented in 1955 by Minsky, [1] the widespread use of confocal imaging was not possible until the invention of lasers and the availability of significant computing power. [2-6] Laser scanning confocal microscopes (LSCMs) use collimated laser light as a 'point' illumination source, with point focus on the sample, and focus the reflected, transmitted, or fluoresced light through a pinhole to provide a 'point' detector. The pinhole defines a second crossover focal point and serves as a wide-angle filter to the detector. If scattered light does not pass through the pinhole, then it is not in focus. Once the light passes through the pinhole, it is typically split into different wavelengths using dichroic mirrors and filters, and then detected by photomultiplier tubes (PMTs). Imaging of large areas of the sample is achieved by raster scanning the beam across the sample using mirrors controlled by piezoelectric actuators (Figure 1).

This paper is arranged as follows. The equipment is briefly described, after which

several examples using different imaging modalities that exploit the advantages of confocal microscopy are shown. The advantage of using a hot stage in a confocal microscope, and of adding a high-resolution spectrometer for photo-stimulated luminescence imaging is also addressed.

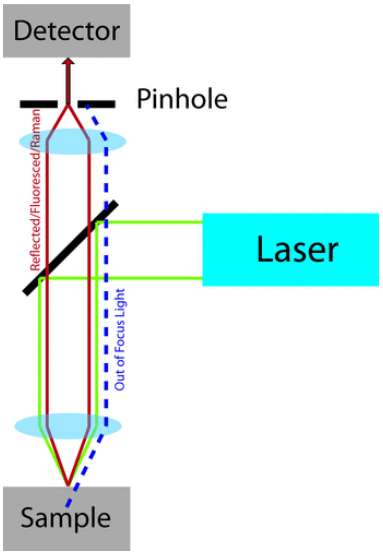

Figure 1:. The optical path of a confocal microscope. The use of point focus and a pinhole aperture located at a crossover focal point (i.e., the confocal point), before the detector provides superior rejection of out-of-focus light. The detector section can be one or more PMTs and/or a spectrometer.

METHODS

All of the data presented in this paper were obtained with an Olympus FV1000 filter-based confocal scan head coupled to an Olympus BX62 upright motorized microscope (Olympus Corp., Tokyo, Japan). Four lasers provide a total of six different wavelengths (405, 458, 488, 514.5, 543, and 633 nm), which can be combined into a single beam before imaging. For reflected light imaging, we prefer the 405 nm laser, as the optical resolution is directly proportional to wavelength. The FV1000 scan head is equipped with three PMTs for reflected/fluoresced light, one PMT for transmitted (non-confocal) light, an Acton 2300i 0.3 m spectrometer (Princeton Instruments, Acton, MA, U.S.A.) equipped with a Princeton Instruments PIXIS 100BR back-illuminated, deep depletion, thermoelectrically cooled charge-coupled device detector (Princeton Instruments, Trenton, NJ, U.S.A.).

RESULTS AND DISCUSSION

Traditionally, to get the highest lateral resolution from a metallurgical microscope, samples had to be polished to a high degree of flatness and then lightly etched to provide optical contrast. If the sample was not perfectly flat or was over-etched, it became difficult or impossible to obtain high-quality optical images. With conventional brightfield optical microscopy, in-focus regions are crisp and clear, whereas out-of-focus regions are less distinct. [7] In con-

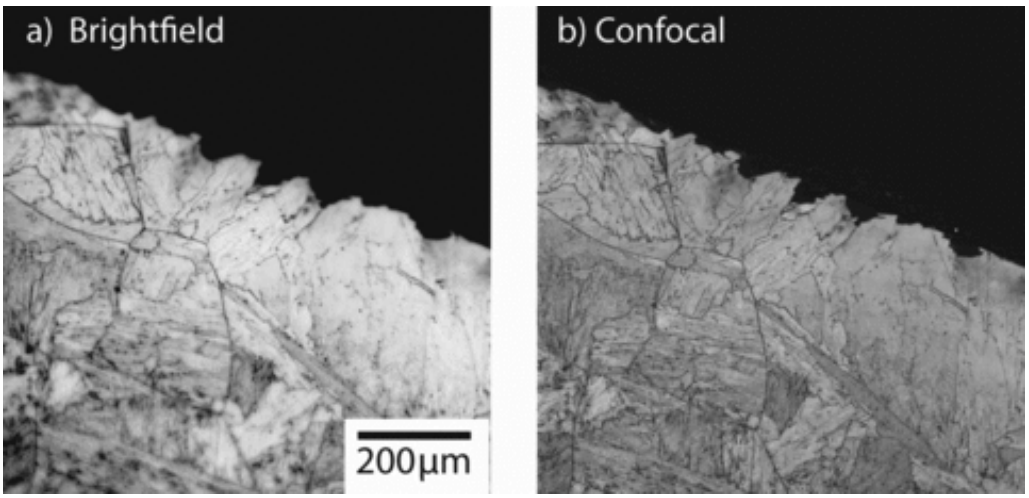

Figure 2:. (a) Conventional brightfield optical micrograph of a polished and etched PH13–8Mo martensitic stainless steel. (b) An image of the same region taken using the 405 nm laser in the laser-scanning confocal imaging reflection mode.

focal microscopy, in-focus regions are similarly crisp and clear, but the intensity in out-of-focus regions drops rapidly. [2-4] As a result, little to no signal is obtained from out-of-focus regions. When combined with a motorized focusing mechanism, it is relatively simple to take a series of images at different focal planes and form a composite image to obtain an 'infinite depth-of-field' image. For a well-prepared metallographic sample, such as the polished PH13–8Mo martensitic stainless steel shown in Figure 2, the confocal image is noticeably sharper, but the actual increase in resolution is modest.

Confocal microscopy has much more significant advantages for samples that cannot be polished to a flat surface. For example, the surface of a sintered aluminum oxide (Al_2O_3) sample was imaged without further specimen separation using brightfield optical microscopy, and it is difficult to resolve the microstructure clearly because of the narrow depth of field of a high numerical aperture objective (Figure 3a). With laser scanning confocal imaging, however, the depth of field becomes slightly smaller, but the out-of-focus regions are dark (Figure 3b). Multiple images can be obtained over a range of focal planes; collecting all the in-focus data and combining the maximum intensity pixels yields an essentially infinite depth-of-field image (Figure 3c). Further, in the process of obtaining adequate images to provide an infinite depth-of-field micrograph, sufficient information is also gathered to produce a topographic map of the sample surface (Figure 4).

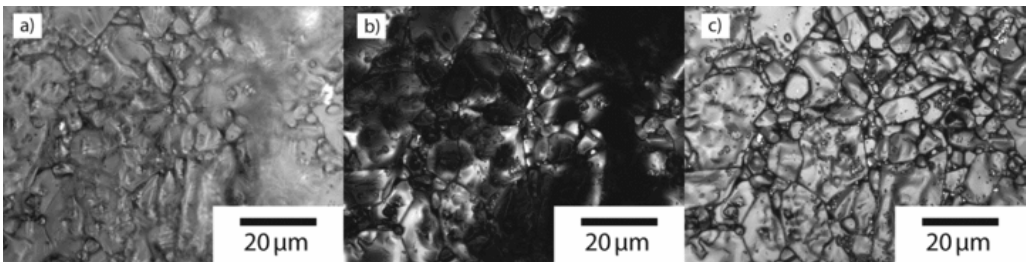

Figure 3:. (a) Conventional brightfield optical micrograph of a sintered Al_2O_3 sample. (b) Single confocal image (405 nm laser) of the same specimen. (c) An 'infinite depth-of-field' confocal image of the same region. This image was acquired by taking 441 images and changing the focal plane by 20 nm between each image and creating a maximum-intensity projection.

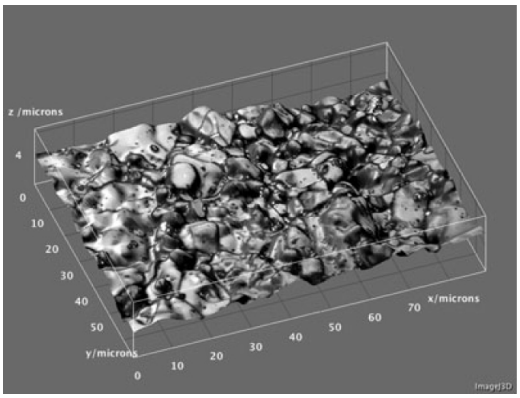

Figure 4:. A 3D topographic model of the surface of the sintered Al_2O_3 sample in Figure 3. The infinite depth-of-field image has been projected onto the modeled surface. The z-axis has been exaggerated by a factor of 2 to highlight the topographic features.

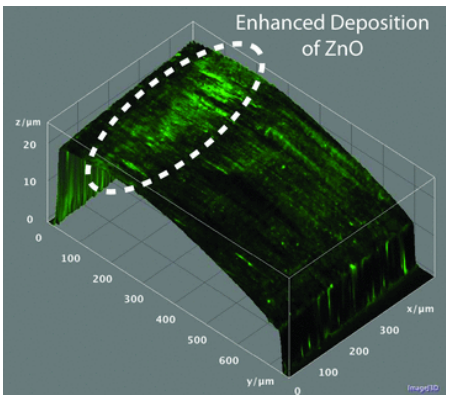

Figure 5:. A three-dimensional model of a piston ring used in an engine. The regions experiencing more wear had increased deposition of zinc oxide (ZnO), which can be recognized by the green fluorescence when stimulated with a 405 nm laser.

For materials scientists, many ceramics, semiconductors, and polymeric materials can provide strong fluorescence, although metals do not fluoresce. By using multiple PMTs, wavelength-specific dichroic mirrors, and bandpass wavelength filters in front of the PMTs, it is possible to image with reflected and fluoresced light simultaneously. An example of this is given in Figure 5, where a piston ring removed from an engine was imaged using both reflected and fluoresced light. The lubricant from the engine deposited ZnO on the piston ring, which is visible as a green fluorescent signal when imaged with the 405 nm laser. By simultaneously imaging with both the reflected laser and the fluoresced radiation, it is possible to obtain a topographic image (from reflected light) and two infinite depth-of-field images (from reflected and fluoresced light, respectively). The infinite depth of field fluorescence image shows a bright band corresponding to increased ZnO deposits. By taking a 3D model of the surface and applying the fluorescence image as a texture, it is possible to see clearly where the greatest deposits of ZnO occurred.

α-alumina (α-Al_2O_3) has strong fluorescence in response to visible laser illumination if trace quantities of chromium are present. In practice, this means that any α-alumina samples, short of a semiconductor-grade sapphire wafer, fluoresce under laser irradiation. This fluorescence is known as the 'ruby' fluorescence and occurs as a peak doublet around 693 nm, known as the R1/R2 doublet. The specific wavelengths of the two peaks are

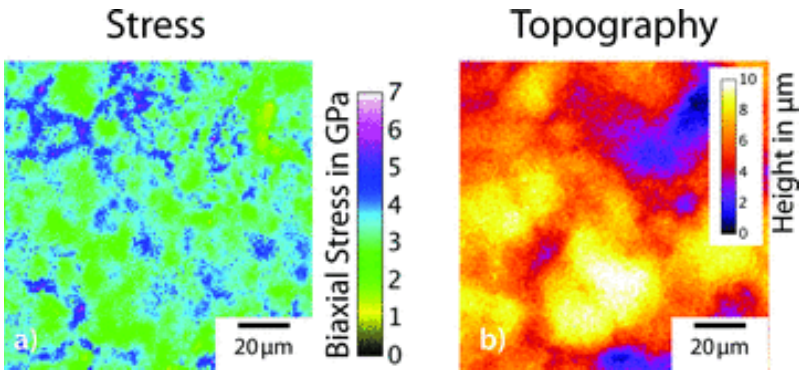

Figure 6: (a) Stress map generated from the R2 fluorescence of the TGO formed on a nickel- platinum-aluminum (NiPtAl) bond coat after 24 one-hour cycles at 1100 °C (2012 °F). (b) The topographic map from the same region.

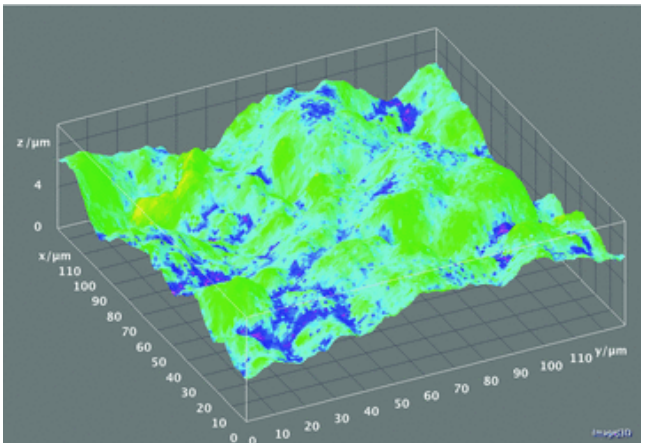

Figure 7:. A 3D model of the surface from Figure 6b, with the stress map projected onto the surface. The regions with downward curvature have lower stress, whereas the regions with upward curvature have greater stress.

stress-sensitive, with the R2 peak being sensitive only to the trace of the stress tensor. The R2 peak shift of ruby has long been used to calibrate the pressure in diamond anvil cells, and the piezospectroscopic coefficients are well established. [8-10] Via spectroscopic analysis of photo-stimulated luminescence in LCSM measurements, stress maps of materials surfaces can be generated, which we call confocal photo-stimulated microscopy (CPSM). [10]

Platinum-modified nickel aluminide (β-phase NiPtAl alloys) bond coats on Ni-base single crystal superalloys have been the subject of extensive studies because of the propensity of these coatings to 'rumple' upon thermal cycling. [11-16] This rumpling can increase the heat transfer from the thermal barrier coating to the underlying metal substrate, accelerating the degradation of structural components. It has also been predicted that the rumpling may affect the stresses in the thermally grown oxide (TGO), leading to premature spallation of the thermal barrier coating. Previous modeling using finite element analysis had predicted that large stress variations would be present due to topography of the TGO, with 'peaks' being less compressive and 'valleys' being more compressive. [17,18] A NiPtAl bond coat on a René N5 superalloy was thermally cycled for 24 one-hour cycles at 1100 °C (2012 °F). A topographic map was obtained by operating the LSCM instrument in reflected-light mode. A series of images were taken at various focal planes to reconstruct the surface topography (Figure 6b). Without moving the sample, a CPSM stress

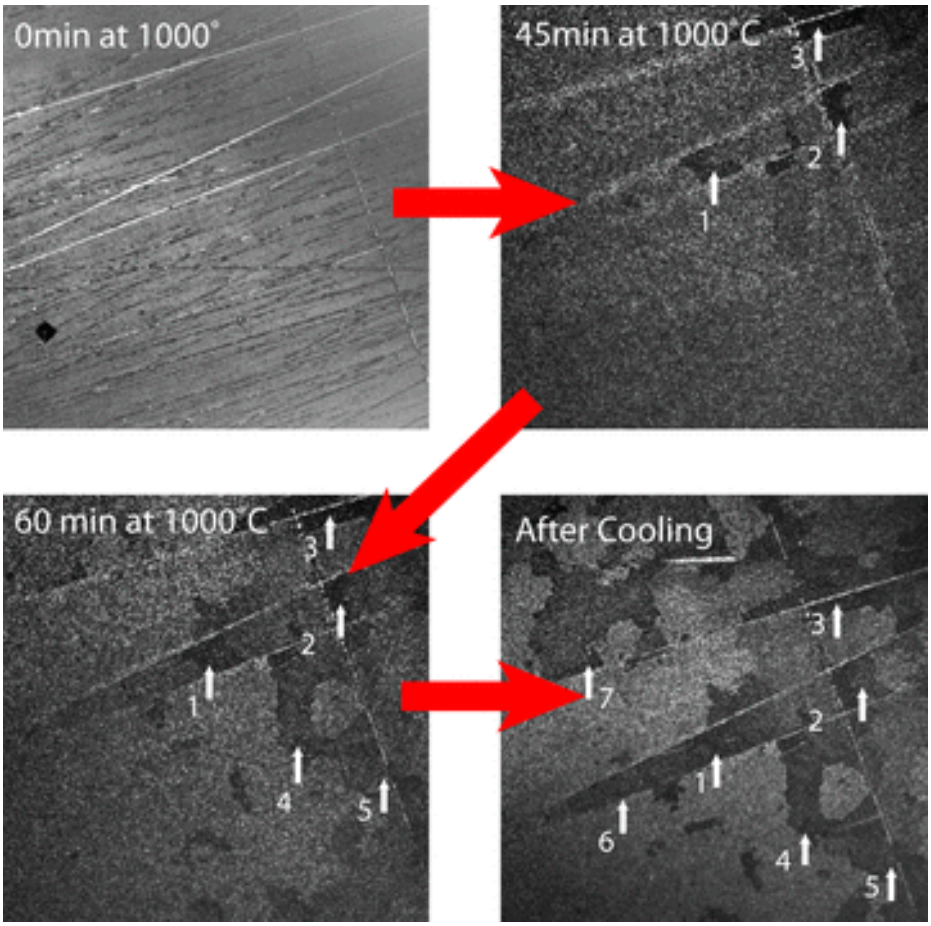

Figure 8:. The progression of a transformation front within an oxide scale across a γ-phase NiCrAl alloy oxidized at 1000 °C (2012 °F) using a hot stage. A 405 nm laser was used for imaging in reflection mode. An oxidation front can be seen progressing across the sample. Transformed regions showing dark contrast are denoted with numbered white arrows.

map was obtained (Figure 6a). Comparing Figure 6a to 6b, a correlation is evident between the topography and the residual stress in the TGO. This can be confirmed by using the topographic data to create a 3D model of the surface. The stresses measured from the same region can then be projected onto this surface as a texture, and as shown in Figure 7, an apparent correlation between topography and residual stress is obtained. The stresses are less compressive in the areas with downward curvature and more compressive where the curvature is upward, providing agreement with previous finite element models. [17,18]

A hot stage attachment is a useful addition to LSCM. Generally, with high-temperature optical imaging, incandescence significantly degrades the image quality. With LSCM, a short wavelength of 405 nm laser can be used for imaging; combined with wavelength filters in the detector section, incandescence can be eliminated. The result is image quality at elevated temperatures that is equivalent to that at room temperature.

An example of hot stage imaging on our LSCM is shown in Figure 8. A γ-phase NiCrAl alloy was oxidized at 1000 °C (2012 °F) and held for 60 min. Upon reaching the oxidation temperature, a 'reaction front' was observed to progress across the surface. At the conclusion of the experiment, the hot stage was cooled at 100 °C min^{-1} (212 °F min^{-1}) to freeze in the feature of interest. As can be seen in Figure 8, the reaction front progressed only modestly as the sample returned to room temperature.

CONCLUSIONS

In conclusion, the confocal microscope is a very useful tool for materials scientists. The microscope can provide the pseudo-infinite depth-of-field imaging of a scanning electron microscope, without the need for a vacuum system or the coating of non-conductive samples. At the same time, topographic capabilities of a profiliometer or atomic force microscope are possible, along with fluorescence imaging, and photo-stimulated luminescence spectroscopy (the CPSM mode). These capabilities make the confocal microscope a versatile addition to the materials science characterization toolkit.

REFERENCES

[1] *M. Minsky, Scanning 1988, 10, 128–138.*

[2] *D.K. Hamilton, T. Wilson, Appl. Phys. B-Photo. 1982, 27, 211– 213.*

[3] *K. Carlsson, P.E. Danielsson, R. Lenz, A. Liljeborg, L. Majlof, N. Aslund, Opt. Lett. 1985, 10, 53–55.*

[4] *K. Carlsson, N. Aslund, Appl. Optics 1987, 26, 3232–3238.*

[5] *G. Q. Xiao, T.R. Corle, G.S. Kino, Appl. Phys. Lett. 1988, 53, 716–718.*

[6] *W. Amos, J. White, Biol. Cell 2003, 95, 335–342.*

[7] *R.C. Gifkins, Optical Microscopy of Metals, American Elsevier Publishing Company, Inc., New York 1970.*

[8] *L. Grabner, J. Appl. Phys. 1978, 49, 580–583.*

[9] *J. He, D.R. Clarke, J. Am. Ceram. Soc. 1995, 78, 1347–1353.*

[10] *D.B. Hovis, A.H. Heuer, Scr. Mater. 2005, 53, 347–349.*

[11] *P.K Wright, A.G. Evans, Curr. Opin. Solid State Mater. Sci. 1999, 4, 255–265.*

[12] *V.K. Tolpygo, D.R. Clarke, Acta Mater. 2000, 48, 3283–3293.*

[13] *V.K. Tolpygo, D.R. Clarke, Acta Mater. 2004, 52, 5115–5127.*

[14] *V.K. Tolpygo, D.R. Clarke, Acta Mater. 2004, 52, 5129–5141.*

[15] *A.G. Evans, D.R. Mumm, J.W. Hutchinson, G.H. Meier, G.S. Pettit, Prog. Mater. Sci. 2001, 46, 505–553.*

[16] *D.R. Mumm, A.G. Evans, I.T. Spitsberg, Acta Mater. 2001, 49, 2329–2340.*

[17] *C.H. Hsueh, J.A. Haynes, J.A., M.J. Lance, P.F. Becher, M.K. Ferber, E.R. Fuller, S.A. Langer, W.C. Carter, W.R. Cannon, J. Am. Ceram. Soc. 1999, 82, 1073–1075.*

[18] *C.H. Hsueh, E.R. Fuller, Mater. Sci. Eng. A 2000, 283, 46–55.*

02 A Novel Slicing Method for Thin Supercapacitors

Hao Sun, Xuemei Fu, Songlin Xie at al.

ABSTRACT

Thin and flexible supercapacitors with low cost and uniform thicknesses were fabricated by a new and efficient slicing method. The morphology of the thin supercapacitors was analyzed by scanning electron microscopy and laser scanning confocal microscopy, which revealed uniform thicknesses and well-formed interfaces between the electrode and the gel electrolyte. Tunable output voltages and energies were realized with a maximum specific capacitance of 248.8 F g^{-1} or 150.8 F cm^{-3}. The devices showed a maintained 96% of the maximum specific capacitance after 300 cycles, and 91% specific capacitance retention when bent to a maximum angle of 180°.

INTRODUCTION

In recent years flexible and miniature electronic devices have accelerated the development of new energy storage systems.[1] Thin energy storage devices have shown promise in a variety of applications, including miniature robotics, implanted microelectronics, and wearable electronics.[1–12] Several strategies, such as photolithography, sputtering, laser scribing, and chemical vapor deposition, have been investigated for the fabrication of miniature electronics.[13–26] Despite the recent achievements, it remains challenging to realize uniform, neat, and low-cost fabrication of thin energy storage devices.

A slicing technique, which uses a sharp blade to cut bulk materials into thin slices, presents a general and efficient method that has been adopted in various fields. In biological and medical sciences, ultrathin slices of tissues and organs are obtained using a microtome.[27,28] Slicing offers low cost, controllable thickness, and small individual variation. However, it is rare to use slicing for microelectronic devices as there remain several challenges, including the difficulty in selecting suitable materials, instability for the interface between different components, and complexity in the design of device structure.

Herein, a new slicing method is developed for fabricating thin supercapacitors with low cost and individual variation. The fabrication of the thin supercapacitor is illustrated in Figure 1. Briefly, aligned multiwalled carbon nanotube (MWCNT) arrays with or without polyaniline (PANI) as electrodes and poly(vinyl alcohol) (PVA)/H_3PO_4 as the gel electrolyte. The aligned MWCNT electrodes allow electrons to hop from one MWCNT to the neighboring others based on a 3D hopping mechanism.[29,30] The composites are embedded in epoxy resin, followed by cutting, using a microtome, into thin supercapacitors that are composed of many supercapacitor units. The thin supercapacitors are tunable in thickness,

demonstrate uniform surfaces, and have compact interfaces for excellent electrochemical properties, e.g., a high specific capacitance of 248.8 F g^{-1} (150.8 F cm^{-3}). This slicing method can be generally applied to the fabrication of other thin energy and electronic devices.

METHODS

Aligned MWCNT arrays with an average height of 1 mm were vertically grown on silicon wafers via chemical vapor deposition. These arrays were uniaxially pressed with a precleaned glass slide and then removed from the substrate with a sharp blade.[31,32] To prepare the aligned MWCNT/PANI composites, the MWCNT film was immersed in an aqueous electrolyte containing 0.1 M aniline and 1 M sulfuric acid and polymerized electrochemically at a potential of 0.75 V using platinum wire counter electrode (CHI115, a diameter of 0.5 mm (0.02 in.)) and a silver/silver chloride (Ag/AgCl)l reference electrode (CHI111, a diameter of 4 mm).[33] The weight percentage of PANI was 70%, which was controlled by assuming an average of 2.5 electrons per aniline monomer. The resulting composite film was twice washed with deionized water and dried in the air before use.

The supercapacitors were fabricated by coating the MWCNT electrodes with PVA/ phosphoric acid (H_3PO_4)and treating in vacuo for 10 min to enhance the infiltration of the electrolyte into the electrodes. The above process was repeated at least two times. Next, the two electrodes were stacked together along the MWCNT-aligned direction to form a thin film supercapacitor. Each electrode shared a width of approximately 110 µm, and the distances between two electrodes ranged from 400 µm – 600 µm.

The stacked films were successively immersed in embedding solutions in acetone. The embedding solution was prepared by mixing an epoxy resin (SPI-PON 812) with T-168 (Shenyang Southeast Chemical Institute) as a plasticizer, dodecenyl succinic anhydride and methyl-5-norbornene-2,3-dicarboxylic anhydride (SPI Supplies Division of Structure Probe, Inc.) as curing agents, and 2,4,6-tris (dimethylaminomethyl phenol) (SPI Supplies Division of Structure Probe, Inc.) as a curing catalyst. Then the composite was put under vacuum to remove air bubbles.[34] It was then placed in a ribbon-shaped mold containing an embedding solution and cured at 60 °C (140 °F) for 24 h. The resulting sample was removed from

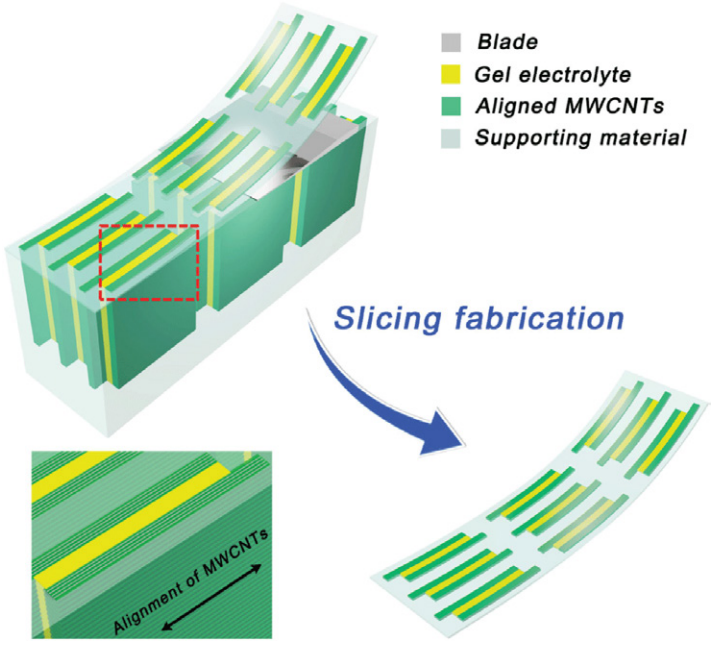

Figure 1: Schematic illustration depicting the fabrication of thin supercapacitors via the slicing method. The left bottom image is the magnified area of the dashed rectangle, showing the alignment of the MWCNTs.

the mold and fixed on the microtome sample stage. A tungsten carbide disposable blade (Leica TC65, a length of 65 mm, or 2.56 in.) was used to cut the thin supercapacitors along the direction of the aligned MWCNTs.

The structures were characterized by an Olympus® LEXT™ OLS4100 laser scanning confocal microscope and scanning electron microscopy (Hitachi FE-SEM S-4800 operated at 1 kV). The thicknesses were measured using a stylus profilometer (Veeco Dektak 150). The electrical resistances were measured using a Keithley 2400 Source Meter. Electrochemical measurements and depositions were performed using an electrochemical workstation (CHI 660E). The cyclic stability was characterized by Arbin electrochemical cycler (MSTAT-5 V/10 mA/16 Ch).

RESULTS

The slicing method enabled a controllable tuning of the device thickness from 10 µm – 60 µm. The gel electrolyte was in close contact with the aligned MWNCTs (Figure 2a). Close contact between the electrode and epoxy resin was also verified (Figure 2b), which is vital for the device to bend without breaking.

Furthermore, the 3D surface topography of the thin supercapacitor was characterized by laser scanning confocal microscopy. Figure 2c shows the reflection mode micrograph from laser scanning confocal microscopy. The green arrow indicates the interface between the MWCNT electrode and the gel electrolyte, and the red arrow indicates the interface

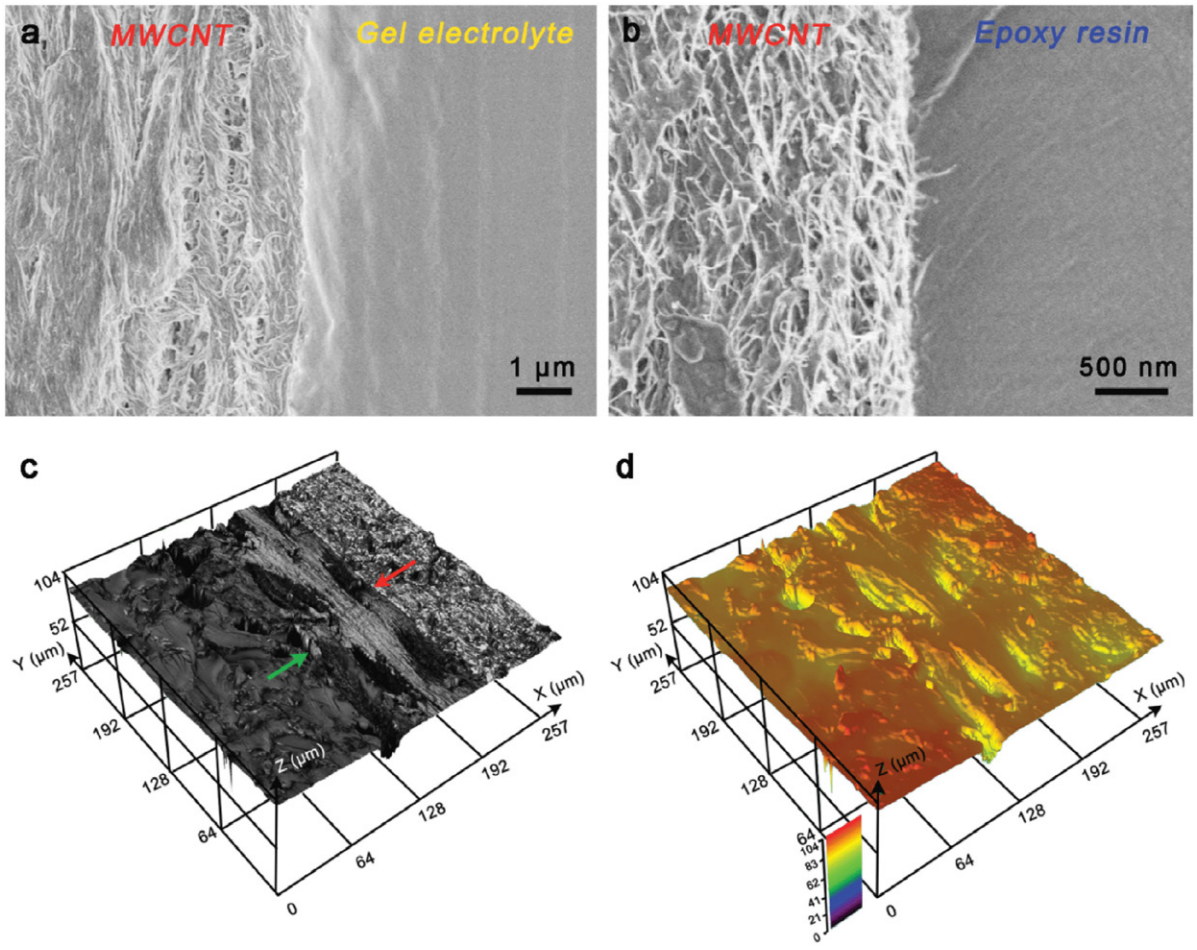

Figure 2: SEM micrographs of a) the interface between the MWCNT electrode and the gel electrolyte, and b) the interface between the MWCNT electrode and the epoxy resin. c) Reflection laser scanning confocal image of the interface in the thin supercapacitor. The green arrow indicates the electrode/electrolyte interface, and the red arrow indicates the electrode/epoxy resin interface. d) Height map of the thin supercapacitor obtained by laser scanning confocal microscopy.

between the electrode and the epoxy resin. Laser scanning confocal microscopy shows that the interfaces in the device are well-formed and relatively defect-free. Figure 2d shows the height map obtained from laser scanning confocal microscopy. The results show a uniform thickness without apparent defects at the interfaces, which is essential for high-performance electronic devices. The uniform surface and compact interfaces are attributed to the high compatibility of the constituent components.

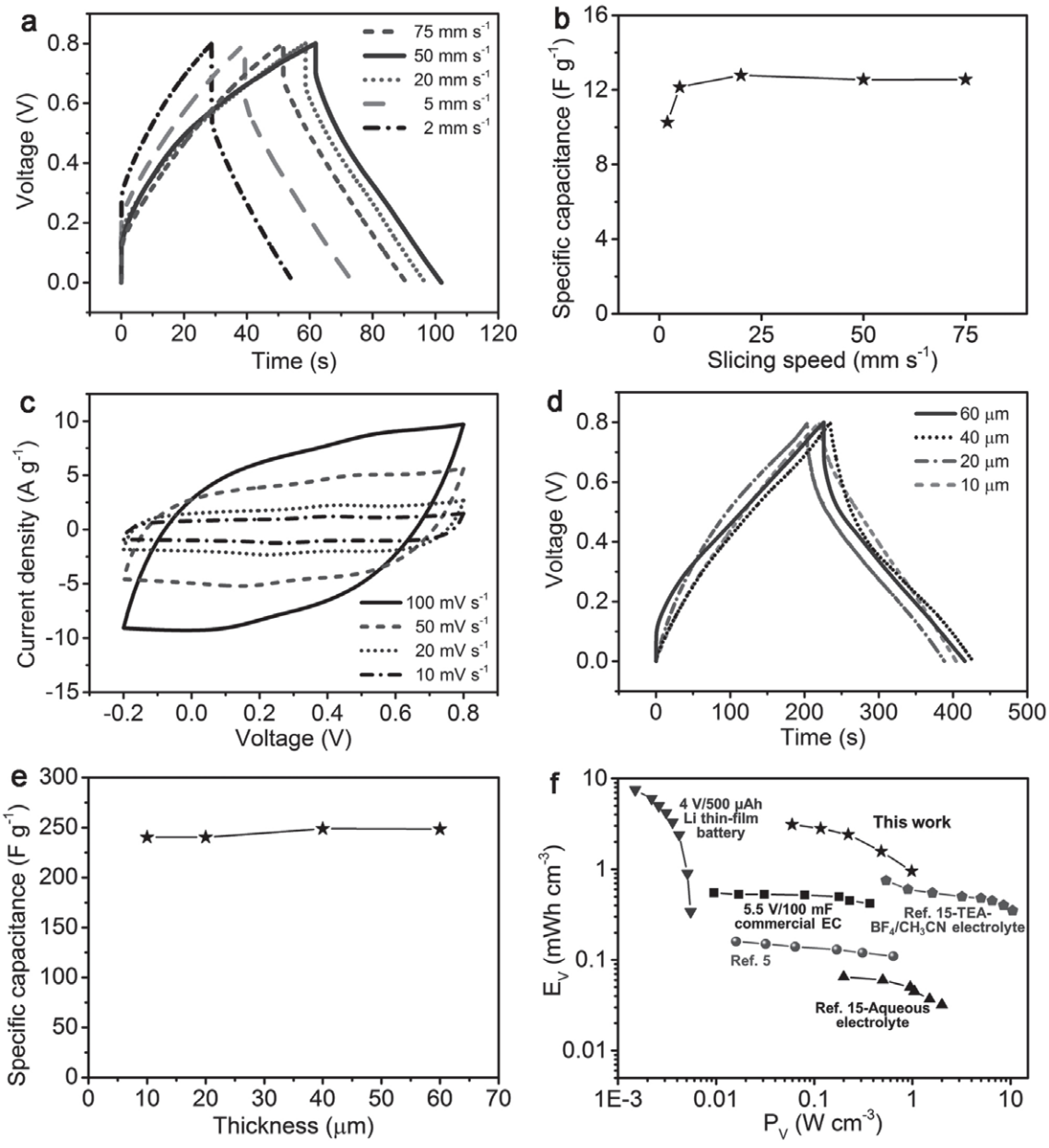

Figure 3: a) Galvanostatic charge-discharge curves for bare MWCNT electrodes at increasing slicing speeds from 2 mm s^{-1} – 75 mm s^{-1} and a current density of 0.15 A g^{-1}. b) Specific capacitance vs slicing speed. c) Cyclic voltammograms for MWCNT/PANI electrodes at different scan rates. d) Galvanostatic charge-discharge curves for thin supercapacitors with aligned MWCNT/ PANI composite electrodes at thicknesses from 10 µm – 60 µm at a current density of 0.50 A g^{-1}. e) The specific capacitance of the thin supercapacitors vs thickness. f) Comparison of the energy and power densities with other energy-storage devices.

The dependence of the specific capacitance on slicing speed was investigated (Figure 3a). The specific capacitances of thin supercapacitors based on bare MWCNTs were increased from 10.3 F g^{-1} to 12.8 F g^{-1} with increasing slicing speed from 2 mm s^{-1} – 20 mm s^{-1} and remained almost unchanged from 20 mm s^{-1} – 75 mm s^{-1} (Figure 3b). This observation may be attributed to the relaxation of polymer chains in the gel electrolyte, which affects the interface with the MWCNTs at different slicing speeds. The relaxation of polymer chains is limited at higher slicing speeds; thus, a better interface between the MWCNT and gel electrolyte is formed, and the device has a lower internal resistance. This phenomenon was also verified by the decreasing internal resistance drop in the galvanostatic charge-discharge curves with increasing slicing speeds (Figure 3a). The specific capacitance reached a plateau at a slicing speed of 20 mm s^{-1}. Therefore, a slicing speed of 20 mm s^{-1} was selected for further studies.

The introduction of PANI increased the specific capacitance of the supercapacitor. For the MWCNT/PANI composite electrodes, reversible charge-discharge performances at a variety of scan rates and current densities were achieved (Figure 3c), and a higher specific capacitance of 240 F g^{-1} (145.5 F cm^{-3}) was achieved. The introduction of PANI increased the specific capacity by approximately 20 times compared to bare MWCNT electrodes. The performance enhancements were attributed to the high conductivity and rapid electron transport that arises from the incorporation of PANI in the porous MWCNT network, the pseudocapacitance associated with the uniformly coated PANI on the surfaces of MWCNTs, and the stable interfaces between the different components to retain high specific capacities after slicing.

For the MWCNT/PANI composites, with the increasing thickness from 10 µm – 60 µm, the galvanostatic charge-discharge was compared at a current density of 0.50 A g^{-1} (Figure 3d). The specific capacitances remained almost unchanged, with a maximum value, at 40 µm, of 248.8 F g^{-1} (150.8 F cm^{-3}) (Figure 3e). The cyclic stability of the thin supercapacitor was verified by cyclic charge-discharge characterization, and the specific capacitance maintained by 96.0% of the maximum value after 2000 cycles. The energy and power densities reached 3.10 mW h cm^{-3} and 0.99 W cm^{-3}, respectively, which are comparable to the previous reports on miniature energy storage devices and commercial counterparts (Figure 3f).[4,5,15,22].

The slicing method shows several unique features that are favorable for practical applications. First, the individual variation of the obtained thin supercapacitors was small. For 22 thin supercapacitors produced under the same conditions, the specific capacitance and internal resistance only varied by 8.8% and 11.6%, respectively (Figure 4a–c). Second, the thin supercapacitors exhibit a low areal density, which is comparable to the state-of-the-art thin energy storage devices and is promising for lightweight electronic devices.[24] Third, they have high flexibility, which is favorable for flexible electronics. The specific capacitance maintained 91% of its maximum value with increasing bending angles from 0° – 180°. It recovered 96% of the specific capacitance after bending at 90° for 300 cycles. The slicing method also enables tunable connectivity of the devices to tune the output voltage and energy. For example, a thin supercapacitor with three units can be connected in series or parallel (Figure 4d), and the output voltage and discharge time were accordingly increased by three times (Figure 4e). As a proof-of-concept lightweight, thin, and flexible power source, a supercapacitor with three serial units was fixed on a fingernail (Figure 4f) to light up a commercial LED (Figure 4g).

CONCLUSIONS

In conclusion, a general and effective slicing method has been developed for the fabrication of thin supercapacitors with low cost and uniform thicknesses. The thin supercapacitors exhibit uniform surfaces, well-formed interfaces, and well-controlled thicknesses. A high specific capacitance of 248.8 F g^{-1} (150.8 F cm^{-3}) was achieved with tunable output voltage and energy. The thin supercapacitors are demonstrated to be lightweight, thin, and flexible power sources to power commercial electronics. This slicing method is also compatible with the fabrication of a variety of other devices including, sensors, transistors, solar cells, and batteries for large-scale production and high performances.

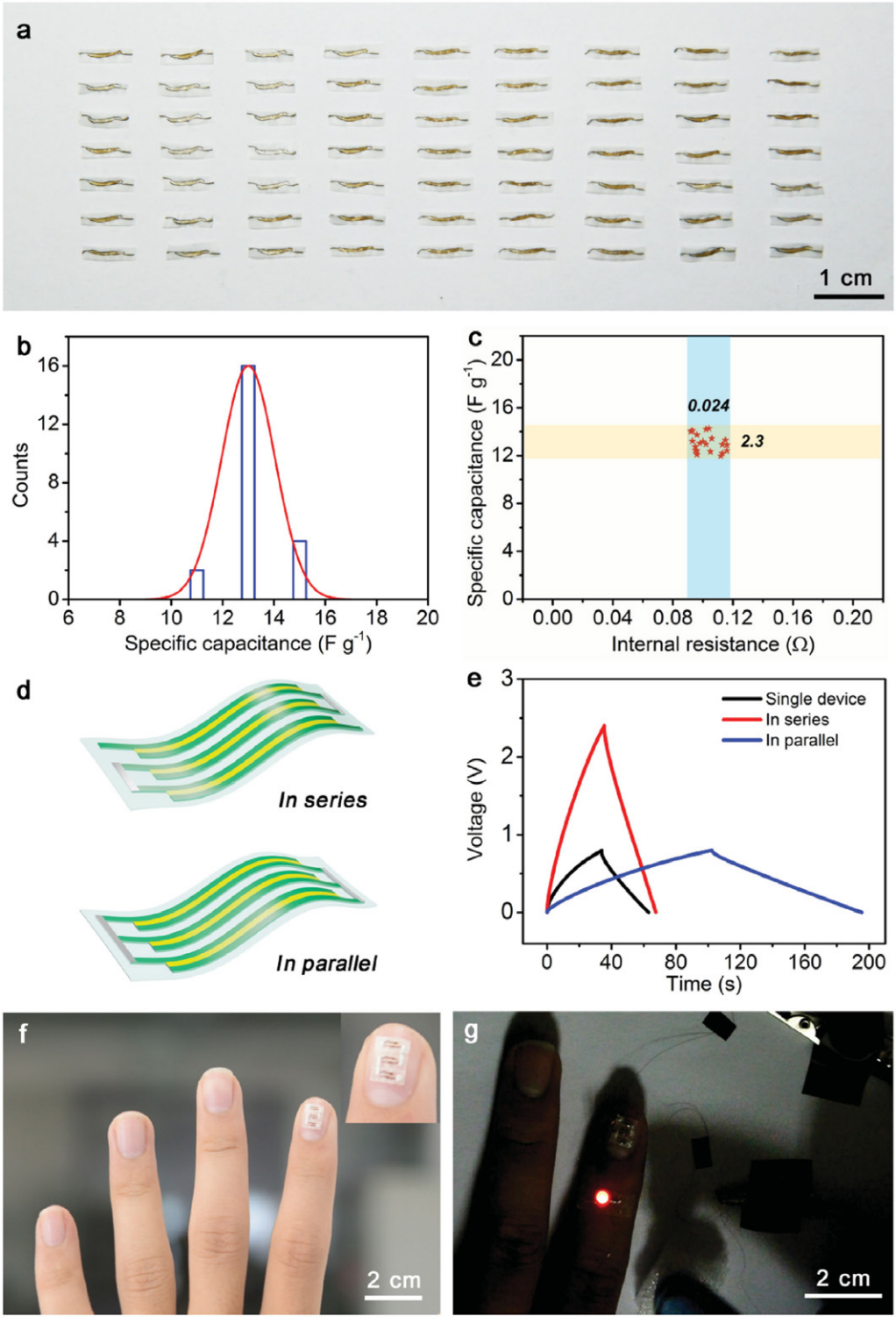

Figure 4: a) Photograph of thin supercapacitors with a thickness of 20 μm and a length of 5 mm (0.2 in.) for each unit. b) Histogram of the specific capacitance of 22 thin supercapacitors fabricated with the same conditions. c) Comparison of the specific capacitance and internal resistance of the 22 thin supercapacitors. d) Schematic illustration of three supercapacitors units connected in series and parallel. e) Galvanostatic charge-discharge curves of one unit, three units connected in series, and three units connected in parallel. Photographs of (f) three units connected in series and placed on a fingernail (g) powering a red LED.

REFERENCES

[1] *M. Beidaghi, Y. Gogotsi, Energy Environ Sci. 2014, 7, 867.*

[2] *J. Chmiola, C. Largeot, P. Taberna, P. Simon, Y. Gogotsi, Science 2010, 328, 480.*

[3] *D. Yu, K. Goh, Q. Zhang, L. Wei, H. Wang, W. Jiang, Y. Chen, Adv. Mater. 2014, 26, 6790.*

[4] *J. Ren, L. Li, C. Chen, X. Chen, Z. Cai, L. Qiu, Y. Wang, X. Zhu, H. Peng, Adv. Mater. 2013, 25, 1155.*

[5] *H. Sun, X. You, J. Deng, X. Chen, Z. Yang, J. Ren, H. Peng, Adv. Mater. 2014, 26, 2868.*

[6] *X. Dong, Z. Guo, Y. Song, M. Hou, J. Wang, Y. Wang, Y. Xia, Adv. Funct. Mater. 2014, 24, 3405.*

[7] *D. Yu, K. Goh, H. Wang, L. Wei, W. Jiang, Q. Zhang, L. Dai, Y. Chen, Nat. Nanotechnol. 2014, 9, 555.*

[8] *D. Yu, S. Zhai, W. Jiang, K. Goh, L. Wei, X. Chen, R. Jiang, Y. Chen, Adv. Mater. 2015, 27, 4895.*

[9] *W. Jiang, S. Zhai, Q. Qian, Y. Yuan, H. E. Karahan, L. Wei, K. Goh, A. K. Ng, J. Wei, Y. Chen, Energy Environ. Sci. 2016. 9, 611.*

[10] *D. Yu, Q. Qian, L. Wei, W. Jiang, K. Goh, J. Wei, J. Zhang, Y. Chen, Chem. Soc. Rev. 2015, 44, 647.*

[11] *M. Yu, Y. Han, X. Cheng, L. Hu, Y. Zeng, M. Chen, F. Cheng, X. Lu, Y. Tong, Adv. Mater. 2015, 27, 3085.*

[12] *M. Yu, Y. Zhang, Y. Zeng, M. S. Balogun, K. Mai, Z. Zhang, X. Lu, Y. Tong, Adv. Mater. 2014, 26, 4724.*

[13] *W. Gao, N. Singh, L. Song, Z. Liu, A. L. M. Reddy, L. Ci, R. Vajtai, Q. Zhang, B. Wei, P. Ajayan, Nat. Nanotechnol. 2011, 6, 496.*

[14] *L. Cao, S. Yang, W. Gao, Z. Liu, Y. Gong, L. Ma, G. Shi, S. Lei, Y. Zhang, S. Zhang, R. Vajtai, P. Ajayan, Small 2013, 9, 2905.*

[15] *M. Kady, S. Veronica, D. Sergey, R. B. Kaner, Science 2012, 335, 1326.*

[16] *Q. Meng, H. Wu, Y. Meng, K. Xie, Z. Wei, Z. Guo, Adv. Mater. 2014, 26, 4100.*

[17] *K. Wang, W. Zou, B. Quan, A. Yu, H. Wu, P. Jiang, Z. Wei, Adv. Energy Mater. 2011, 1, 1068.*

[18] *Z. Wu, K. Parvez, X. Feng, K. Müllen, Nat. Commun. 2013, 4, 2487.*

[19] *Z. Wu, K. Parvez, A. Winter, V. H. Vieker, X. Liu, S. Han, A. Turchanin, X. Feng, K. Müllen, Adv. Mater. 2014, 26, 4552.*

[20] *D. Qi, Z. Liu, Y. Liu, W. Leow, B. Zhu, H. Yang, J. Yu, W. Wang, H. Wang, S. Yin, X. Chen, Adv. Mater. 2015, 27, 5559.*

[21] *Z. Niu, L. Zhang, L. Liu, B. Zhu, H. Dong, X. Chen, Adv. Mater. 2013, 25, 4035.*

[22] *S. Kim, H. Koo, A. Lee, P. Braun, Adv. Mater. 2014, 26, 5108.*

[23] *C. Meng, J. Maeng, S. John, P. Irazoqui, Adv. Energy Mater. 2014, 4, 1301269.*

[24] *Z. Su, C. Yang, B. Xie, Z. Lin, Z. Zhang, J. Liu, B. Li, F. Kang, C. P. Wong, Energy Environ. Sci. 2014, 7, 2652.*

[25] *M. Beidaghi, C. Wang, Adv. Funct. Mater. 2012, 22, 4501.*

[26] *M. Beidaghi, C. Wang, Electrochim. Acta 2011, 56, 9508.*

[27] *A. Igersheim, O. Cichocki, Rev. Palaeobot. Palynol. 1996, 92, 389.*

[28] *W. Han, S. Heo, T. Driscoll, J. Delucca, C. McLeod, L. Smith, R. Duncan, R. Mauck, D. M. Elliott, Nat. Mater. 2016, 15, 477 .*

[29] *T. Chen, S. Wang, Z. Yang, Q. Feng, X. Sun, L. Li, Z. S. Wang, H. Peng, Angew. Chem. Int. Ed. 2011, 50, 1815.*

[30] *H. Peng, M. Jain, D. E. Peterson, Y. Zhu, Q. Jia, Small 2008, 4, 1964.*

[31] *Z. Yang, L. Li, H. Lin, Y. Luo, R. He, L. Qiu, J. Ren, H. Peng, Chem. Phys. Lett. 2012, 549, 82.*

[32] *H. Sun, R. Che, X. You, Y. Jiang, Z. Yang, J. Deng, L. Qiu, H. Peng, Adv. Mater. 2014, 26, 8120.*

[33] *A. Yu, I. Roes, A. Davies, Z. Chen, Appl. Phys. Lett. 2010, 96, 253105.*

[34] *a) L. Li, Z. Yang, H. Gao, H. Zhang, J. Ren, X. Sun, T. Chen, H. G. Kia, H. Peng, Adv. Mater. 2011, 23, 3730 ; b) S. Huang, L. Li, Z. Yang, L. Zhang, H. Saiyin, T. Chen, H. Peng, Adv. Mater. 2011, 23, 4707.*

03 Boosted UV Photodetection Performance in Chemically Etched Amorphous Ga_2O_3 Thin-Film Transistors

Zuyin Han, Huili Liang, Wenxing Huo et al.

ABSTRACT

Bottom-gate amorphous gallium oxide ($Ga_2O_{3)}$ (a-Ga_2O_3) thin-film transistors (TFTs) were fabricated to boost their UV photodetection properties. A simple chemical-etching solution was employed that is easy to use, low cost, and compatible with traditional lithographic processes to selectively etch a-Ga_2O_3 films. The a-Ga_2O_3 channel etched device, on silicon, effectively suppresses gate leakage current. Further, a patterned a-Ga_2O_3 TFT on quartz shows excellent n-type TFT performance with a high on/off ratio of approximately 10^7. It is also applied as a phototransistor, to diminish the persistent photoconductivity (PPC) effect while keeping a high responsivity (R). Under 254 nm UV illumination, the a-Ga_2O_3 phototransistor demonstrated a high light-to-dark ratio of 5×10^7, a high responsivity of $R = 5.67 \times 10^3$ A W^{-1}, and a high detectivity of 1.87×10^{15} Jones. The PPC phenomenon in a-Ga_2O_3 UV phototransistors was effectively suppressed by applying a positive gate pulse, which significantly shortens the decay time to 5 ms and enables possible imaging applications.

INTRODUCTION

Amorphous galium oxide (Ga_2O_3) (a-Ga_2O_3) has attracted increasing attention for its wide range of applications in deep ultraviolet (UV) photodetection, such as confidential space communication, imaging, flame detection, and missile warning systems. [1–4] Two-terminal Ga_2O_3 photodetectors (PDs) are the most commonly investigated, but their slow response speed, caused by persistent photoconductivity (PPC), [5,6] impedes their further application. [7] PPC occurs in most oxide semiconductor materials because of the large quantity of oxygen vacancy (V_o) defects and the high density of trap states. [8,9]

Three-terminal PD, or phototransistors, have an additional terminal-gate to control the channel carriers' transportation behavior are regarded as an alternative solution to improve the PD performance.[10,11] Phototransistors have the

intrinsic gain of transistors and regular photoconductors, which makes it possible to achieve high light-to-dark current ratios and responsivity (*R*).[11,12] PPC can be eliminated by exerting a gate pulse, as demonstrated by Jeon et al. in a three-terminal photosensor array.[5] For a-Ga_2O_3 UV PD or imaging applications, research is needed to suppress PPC and raise the response speed while retaining a *R*. The controllable and selective etching of a-Ga_2O_3 channels to metals and other oxides is critical to achieving a low gate leakage current and favorable transfer characteristics. [13,14] Wet chemical etching of β-Ga_2O_3 has been demonstrated by using phosphoric acid (H_3PO_4) and sulfuric acid (H_2SO_4). [15,16] However, these strong acids readily corrode metals and oxides, which makes device fabrication difficult.

In this study, we present bottom-gate a-Ga_2O_3 thin-film transistors (TFTs) and phototransistors, where the a-Ga_2O_3 channels were selectively etched using tetramethylammonium hydroxide (TMAH) aqueous solution. This new etching method is low cost, simple, safe, and is compatible with conventional lithographic techniques. For the bottom-gate Ga_2O_3 TFT on silicon, the patterned channel device exhibits superior transistor characteristics compared to the unpatterned one. A bottom-gate a-Ga_2O_3 phototransistor with interdigitated source/drain (S/D) electrodes was prepared on quartz and used to detect deep UV rays. It demonstrated typical transistor output and transfer characteristics with a high on/off ratio of approximately 10^7. Meanwhile, excellent photodetector performance was demonstrated under a 254 nm UV illumination, including a high light-to-dark ratio of 5×10^7 and $R = 5.67 \times 10^3$ A W^{-1}. By applying a positive gate pulse, PPC in the a-Ga_2O_3 phototransistors is effectively eliminated with a fast decay in 5 ms.

METHODS

Common-gated a-Ga_2O_3 TFTs were fabricated on silicon dioxide (SiO_2) (300 nm)/Si substrates. An a-Ga_2O_3 channel layer (25 nm) was deposited by RF-sputtering using a Ga_2O_3 ceramic target (99.999% pure) at room temperature and patterned by UV-lithography followed by wet chemical etching in a TMAH solution. The ITO (100 nm) S/D electrodes were prepared by UV-lithography and lift-off process, where the film deposition was carried out in a sputtering chamber. Bottom gate staggered a-Ga_2O_3 TFTs were fabricated on quartz substrates with interdigitated S/D electrodes. Cr film (35 nm) was deposited by RF-magnetron sputtering and wet etched after the lithography to form the bottom gate electrode. Then, aluminum oxide (Al_2O_3) (110 nm) was grown on the gate metal at 200 °C (392 °F) in the ALD system and patterned by the combined process of UV-lithography and wet etching in an H_3PO4 solution. After that, a 25 nm a-Ga_2O_3 layer was sputtered, which is also patterned into discrete rectangles with dimensions of 175 µm × 600 µm. Next, interdigitated S/D electrodes are defined by UV-lithography. The S/D electrodes have 15 pairs of fingers with 10 µm in width, 10 µm in spacing gap, and 145 µm in length. At last, a sequential deposition of tin (Ti) and gold (Au) layers were deposited in the RF-magnetron sputtering system with a thickness of 20 nm and 80 nm, respectively, which are further patterned by the following lift-off process.

Film thickness was measured by a stylus profiler (KLA-Tencor P-6 Stylus Profiler). The surface morphology was evaluated by atomic force microscopy (AFM, Bruker Dimension EDGE), laser scanning confocal microscope (Olympus® LEXT™ OLS5000 system), and scanning electron microscopy (SEM, Zeiss Sigma 300). The electrical properties were analyzed using a Keithley 4200 and a Keithley 6487. A handheld UV 254 nm lamp (ZF-5) and a xenon lamp with Omni-λ 180i grating spectrometer were used.

RESULTS AND DISCUSSION

The etching behaviors of two a-Ga_2O_3 samples were first investigated using different TMAH concentrations and temperatures. The a-Ga_2O_3 films are labeled as S1 and S2, which are sputtered with oxygen (O_2) and without O_2 flux, respectively. Both of the samples are amorphous. S1 and S2 have different densities, determined from X-ray reflection spectra (XRR), which are 5.32 g cm^{-3} (332 lb ft^{-3}) and 4.84 g cm^{-3} (302 lb ft^{-3}), respectively. The density affects the etching rate because of their different Vo defect densities. [8] The etching rates of S1 are slower than S2, which are attributed to its higher density and hence denser structure.

The selective etching ability of a TMAH solution is critical for the fabrication of TFTs. The amorphous Al_2O_3 was immersed in a 0.048% TMAH solution at 27 °C (80.6 °F) for 140 s, the depth profile of Al_2O_3 was almost unchanged, suggesting that it is hardly etched by TMAH at this low concentration. A slight etching of Al_2O_3 does occur, at a rate of 0.72 nm s^{-1}, in a 0.24% TMAH solution at 60 °C for 15 s. Thus, a selec-

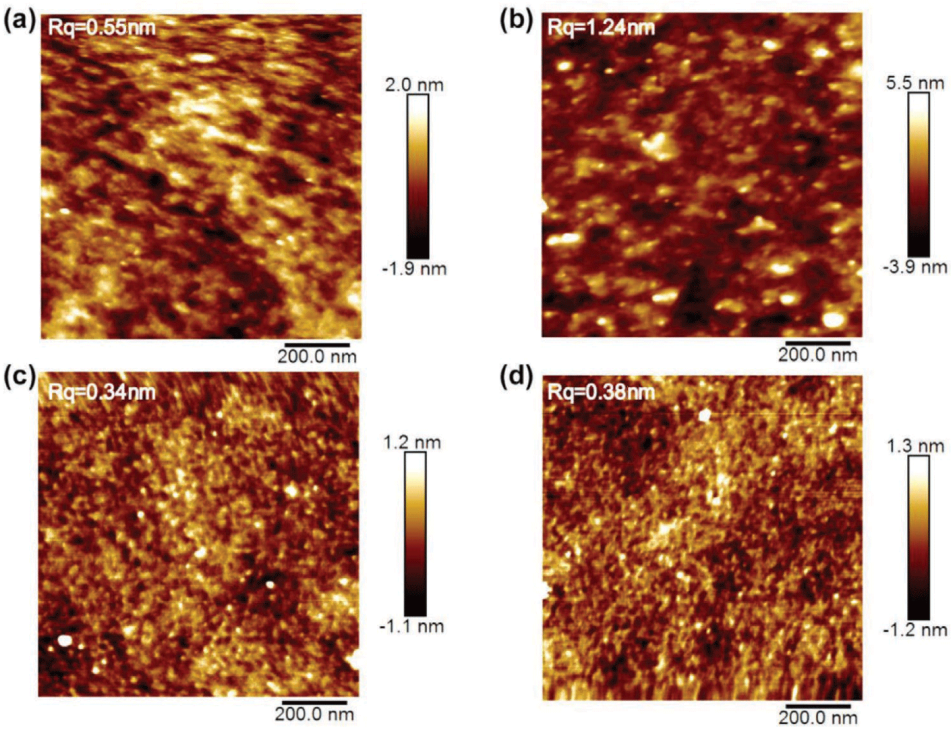

Figure 1: AFM images of a) unetched a-Ga_2O_3 film (S2), b) etched a-Ga_2O_3 film (S2), c) unetched a-Al_2O_3 film, and d) etched a-Al_2O_3 film.

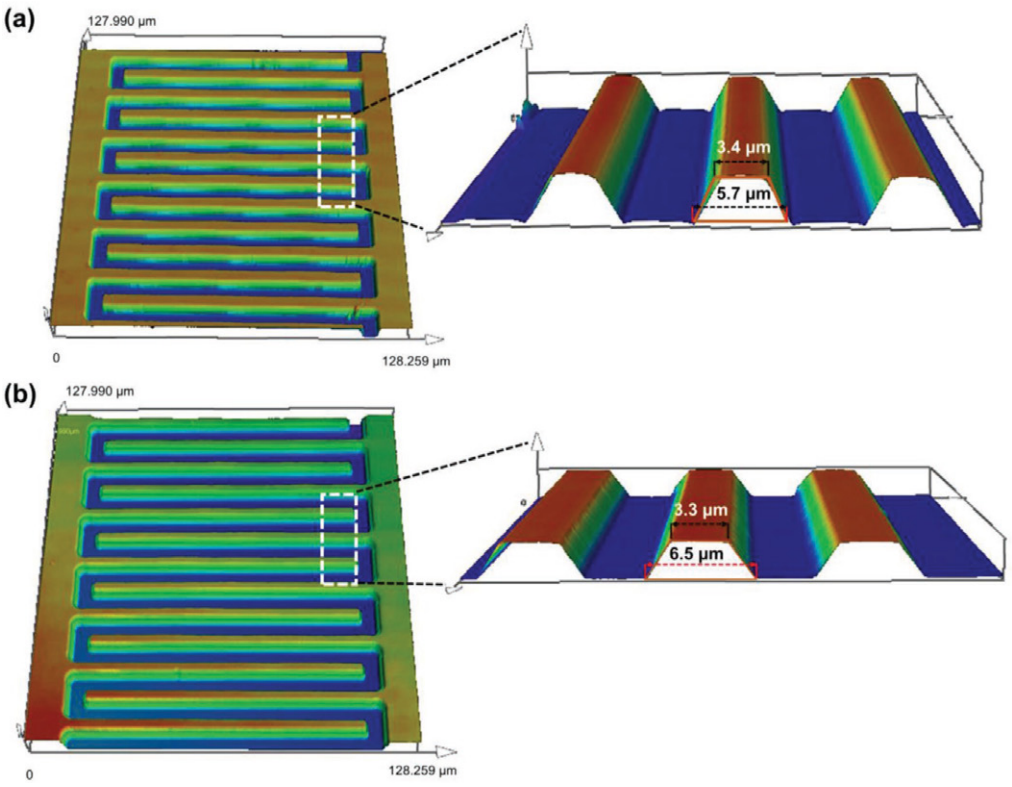

Figure 2: Laser scanning confocal microscope images of a-Ga_2O_3 film etched with a) TMAH solution and b) H_3PO_4 solution.

tive etching rate ratio of a-Ga_2O_3 (S2) to Al_2O_3 of 17:1 in the 0.24% TMAH solution at 60 °C (140 °F) was achieved, which provides an adequately wide and easily controllable operation regime for the fabrication of a-Ga_2O_3 TFTs.

The a-Ga_2O_3 and Al_2O_3 surface morphologies, after being etched, is revealed by AFM (Figure 1). The root-mean-square (RMS) surface roughness of the as-deposited a-Ga_2O_3 (Figure 1a) film is 0.55 nm, which is slightly smaller than the 1.24 nm after etching (Figure 1b). In Figure 1c,d, the RMS values are 0.34 nm and 0.38 nm for unetched and etched Al_2O_3 films, respectively, indicating that the Al_2O_3 surface is uniformly etched by TMAH solution under this condition.

To further corroborate the effect of TMAH solution on the a-Ga_2O_3 patterns, 400 nm thick Ga_2O_3 films were patterned and etched into interdigitated features by etching with TMAH and H_3PO_4 solutions. Figure 2a,b shows the corresponding 3D laser scanning confocal microscope images collected in reflection mode, where well-defined patterns can be clearly seen in both cases. The cross-sectional views show the same trapezoidal structure, which is favorable for metal deposition. The ratios of the top to the bottom edges of the trapezoids are similar, demonstrating that the etching effect of TMAH is comparable with H_3PO_4. Thus, considering that TMAH barely etches metal or Al_2O_3, it is more preferred than H_3PO_4 for the fabrication of multi-component devices.

Based on the above-mentioned wet chemical etching technique using TMAH solutions, common bottom-gate TFTs with patterned and unpatterned a-Ga_2O_3 channels were fabricated on commercial SiO_2/Si substrates (Figure 3a). The electrical characteristics are measured at a source-drain voltage (VDS) of 10 V with the source–gate voltage (VGS) from -100 V – 200 V (Figure 3b). The TFT with patterned a-Ga_2O_3 channel exhibits a typical n-type transfer curve. [17,18] The gate current (I_{GS}), generally defined as leakage current, is very low, about 10^{-10} A for the entire V_{GS} range. Conversely, the TFT with unpatterned a-Ga_2O_3 channel shows an abrupt drop of the drain

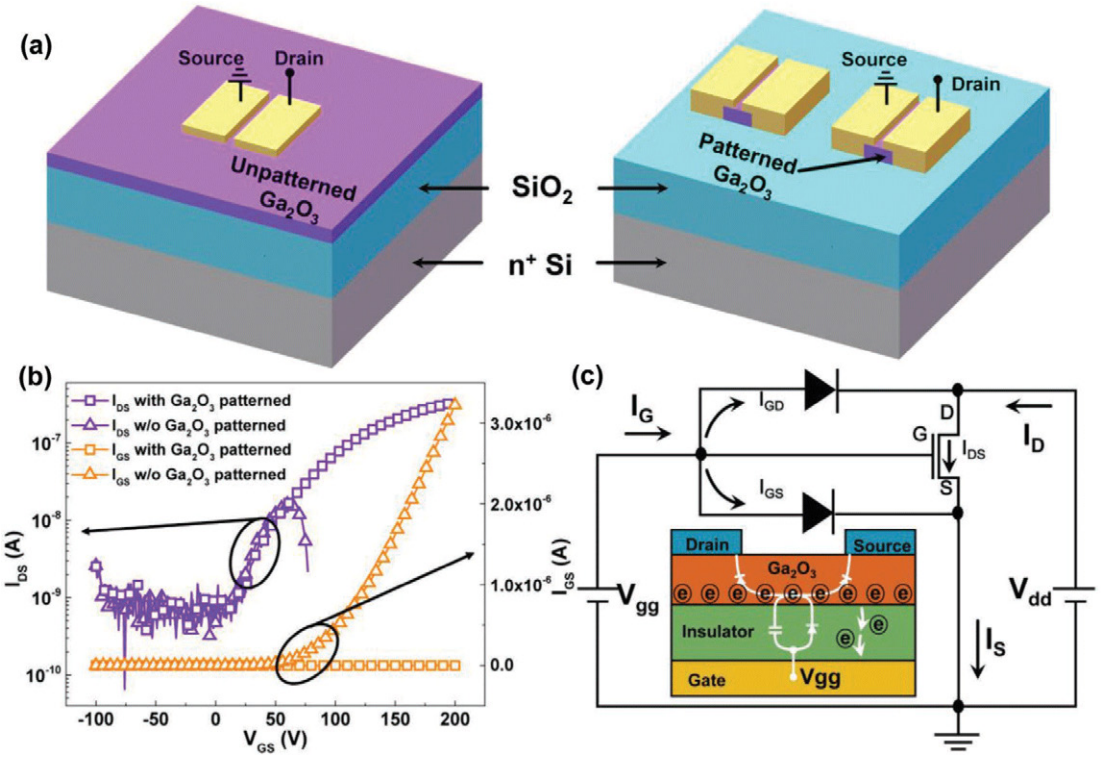

Figure 3: a) Schematic structures of the TFTs. b) I_{DS}–V_{GS} curves and I_{GS}–V_{GS} curves. c) Equivalent circuit of a-Ga_2O_3 TFT without channel patterned.

current (I_{DS}) in the transfer curve at a specific V_{GS}, where the I_{GS} begins to increase dramatically, indicating that the channel electrons start to transport vertically through SiO_2 layer and reach the gate electrode at a positive V_{GS}. The abnormal curves imply that it is beneficial to use a patterned a-Ga_2O_3 channel layer.

Next, an Al_2O_3 dielectric layer was used to fabricate a-Ga_2O_3 TFT with a bottom-gate staggered structure on quartz substrates. The interdigitated configuration is used to separate photogenerated carriers effectively.[1,19] A winding gate electrode was designed with a 1.5 μm overlap at the edge of the S/D electrodes (Fig-

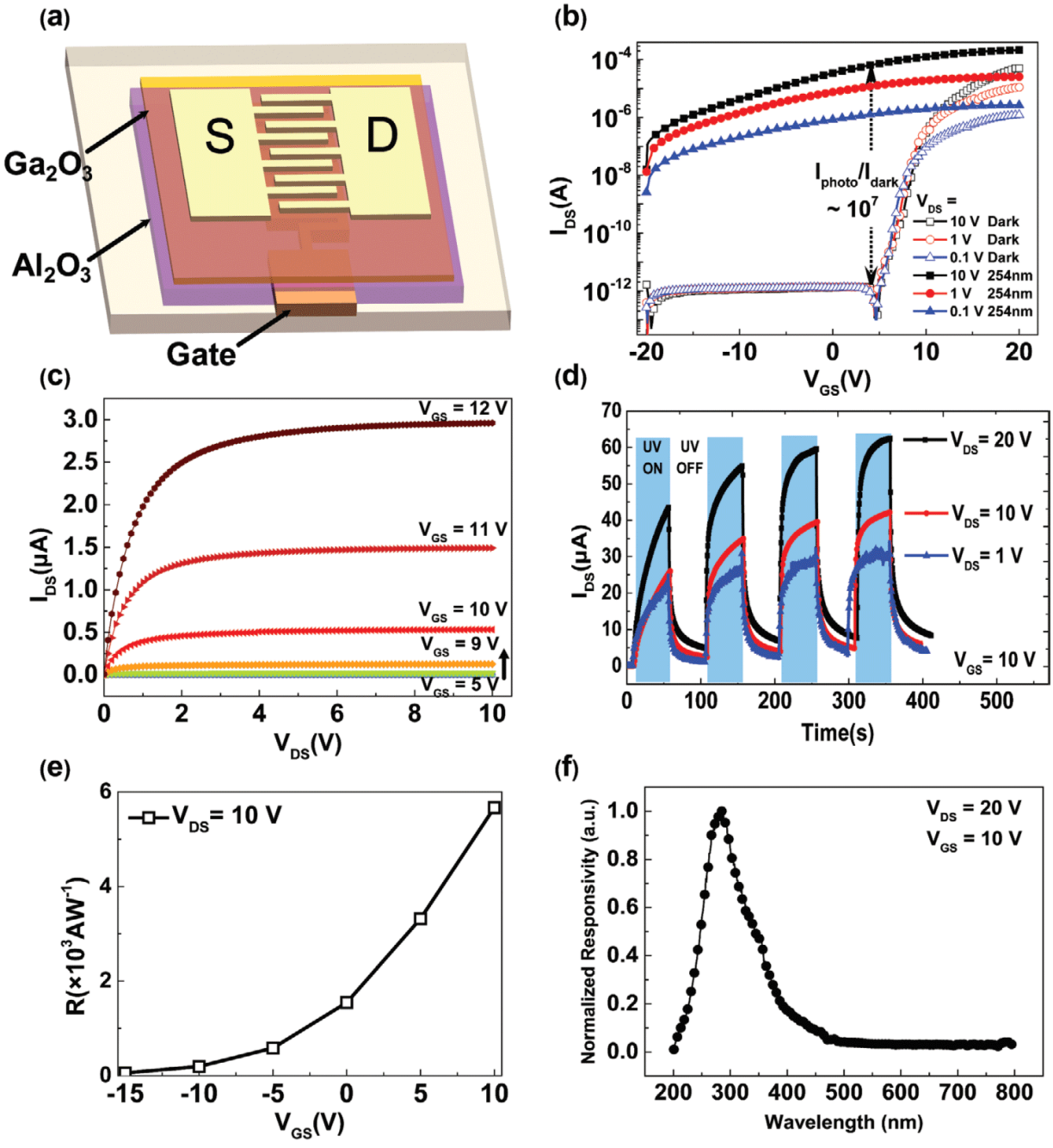

Figure 4: a) Schematic structure of the a-Ga_2O_3 phototransistor on quartz. b) I_{DS}–V_{GS} curves, and c) I_{DS}–V_{DS} curves. d) Time-dependent photoresponse curves. e) *R*–V_{GS} curve. f) Normalized photoresponsivity spectrum.

ure 4a). Figure 4b shows the I_{DS}–V_{GS} transfer curves at different VDS in the dark and under 254 nm light illumination. The on-state I_{DS} increases as V_{DS} increases from 0.1 V to 10 V, and the off-state IDS remains low. The device exhibits decent electrical performance, such as a high on/off ratio of about 10^7, a low subthreshold swing of 0.65 mV dec^{-1} and a moderate positive threshold voltage (V_{th}) of 5 V. Under 254 nm light, the I_{DS} increases in the depletion region compared with the inthe dark. The on-state photocurrent also increases as V_{DS} increases from 0.1 V to 10 V. At V_{DS} = 10 V and V_{GS} = 4 V, a high photocurrent of about 10^{-4} A is obtained, leading to a large light-to-dark current ratio of 5×10^7.

The ultrahigh rejection ratio is reasonable because the depletion "off" state in the dark is reversed into an "on" state due to the presence of numerous photogenerated electrons.[20] Figure 4c demonstrates the output curves of the same device with an excellent linear and saturation performance, indicating a good ohmic contact between the Ga_2O_3 and Ti/Au. Time-dependent photoresponse behavior was evaluated with V_{GS} = 10 V (Figure 4d). The I_{DS} increases as V_{DS} varies from 1 V – 20 V. Furthermore, the device demonstrates a relatively slow response to the periodic UV illumination. Figure 4e shows the responsivity (R) as a function of V_{GS} at V_{DS} = 10 V. R is calculated according to the following equation:

$$R=\frac{(I_{photo}-I_{dark})}{PS}$$

where I_{photo} is the photocurrent, I_{dark} is the dark current, P is the light intensity, and S is the illumination area. As V_{GS} increases from –15 V– 10 V, R increases to 5.67×10^3 A W^{-1}. Based on this responsivity value, the detectivity (D^*) expressed as:

$$D^*=\frac{RS^{1/2}}{(2qI_{dark})^{1/2}}$$

is calculated to be 1.87×10^{15} Jones. A normalized photoresponse spectrum has been measured at V_{DS} = 20 V and V_{GS} = 10 V and shows a peak at 285 nm and a long tail until 360 nm. (Figure 4f)

Next, the suppression of PPC with the pulse gate voltage was investigated. A strong PPC remains for dozens or even hundreds of seconds in the a-Ga_2O_3 phototransistor working in a quasi-two-terminal configuration with V_{GS} = 0 V, (Figure 5a), which severely hinders its practical applications. To diminish the PPC, a positive 20 V gate bias with a pulse width of 850 ms is applied. The I_{DS} curve shows an instantaneous sharp peak and then immediately recovers to about 10^{-10} A once the gate voltage is reset to 0 V, suggesting that the PPC phenomenon is suppressed (Figure 5a,b). The decay time τ_d, defined as the time during which the current decays from 90% to 10%, was 5 ms.

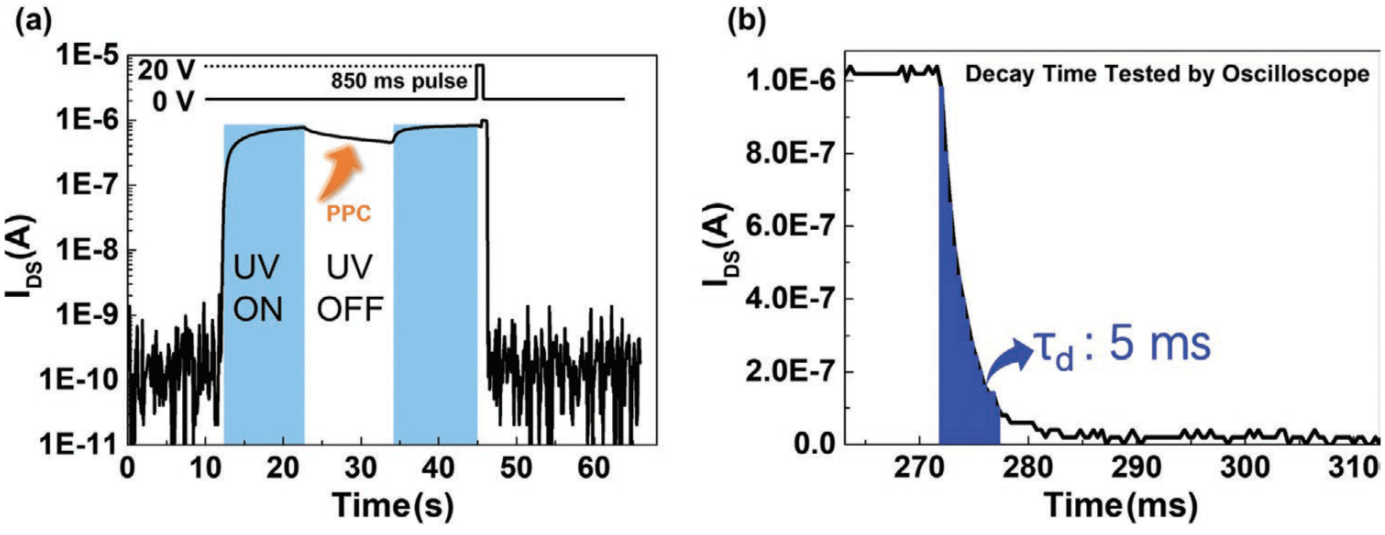

Figure 5: a) Suppression of PPC with a positive gate pulse. b) I_{DS} Decay time.

CONCLUSIONS

In this work, a highly selective etching solution was developed for the preparation of patterned a-Ga_2O_3 films using TMAH. A distinct influence of the chemical etching on device performance is investigated by comparison of two common bottom-gate TFTs with patterned and unpatterned a-Ga_2O_3. Furthermore, a bottom-gate a-Ga_2O_3 TFT was fabricated, with interdigitated S/D electrodes. The TFT shows typical n-type oxide semiconductor TFT transfer curves with a high on/off ratio of approximately 10^7, and excellent output characteristics. The device demonstrates a good response to UV 254 nm light, such as a high light-to-dark ratio of 5×10^7 and responsivity of 5.67×10^3 A W^{-1}. Also, the PPC in a-Ga_2O_3-based phototransistors is effectively suppressed by applying a positive gate pulse with a decay time as low as 5 ms. These results suggest that the chemically etched a-Ga_2O_3 phototransistor is promising for high-performance UV photodetection and imaging applications.

REFERENCES

[1] *S. Cui, Z. Mei, Y. Zhang, H. Liang, X. Du, Adv. Opt. Mater. 2017, 5, 1700454.*

[2] *S.-J. Cui, Z.-X. Mei, Y.-N. Hou, Q.-S. Chen, H.-L. Liang, Y.-H. Zhang, W.-X. Huo, X.-L. Du, Chin. Phys. B 2018, 27, 067301.*

[3] *S. Cui, Z. Mei, Y. Hou, M. Sun, Q. Chen, H. Liang, Y. Zhang, X. Bai, X. Du, Sci. China: Phys., Mech. Astron. 2018, 61, 107021.*

[4] *N. Kumar, K. Arora, M. Kumar, J. Phys. D: Appl. Phys. 2019, 52, 335103.*

[5] *S. Jeon, S.-E. Ahn, I. Song, C. J. Kim, U.-I. Chung, E. Lee, I. Yoo, A. Nathan, S. Lee, K. Ghaffarzadeh, J. Robertson, K. Kim, Nat. Mater. 2012, 11, 301.*

[6] *H. X. Jiang, J. Y. Lin, Phys. Rev. Lett. 1990, 64, 2547.*

[7] *D. Ye, Z. Mei, H. Liang, L. liu, Y. Zhang, J. Li, Y. Liu, C. Gu, X. Du, Sci. Rep. 2016, 6, 26169.*

[8] *H. Liang, S. Cui, R. Su, P. Guan, Y. He, L. Yang, L. Chen, Y. Zhang, Z. Mei, X. Du, ACS Photonics 2019, 6, 351.*

[9] *A. Jacnotti, C. G. Van de Walle, Phys. Rev. B 2007, 76, 165202.*

[10] *Y. Qin, H. Dong, S. Long, Q. He, G. Jian, Y. Zhang, X. Zhou, Y. Yu, X. Hou, P. Tan, Z. Zhang, Q. Liu, H. Lv, M. Liu, IEEE Electron Device Lett. 2019, 40, 742.*

[11] *Y. Qin, S. Long, Q. He, H. Dong, G. Jian, Y. Zhang, X. Hou, P. Tan, Z. Zhang, Y. Lu, C. Shan, J. Wang, W. Hu, H. Lv, Q. Liu, M. Liu, Adv. Electron. Mater. 2019, 5, 1900389.*

[12] *W. Kim, K. S. Chu, Phys. Status Solidi A 2009, 206, 179.*

[13] *J. Lee, K.-H. Lim, Y. S. Kim, Sci. Rep. 2018, 8, 13905.*

[14] *K. Seong, K. Kim, S. Y. Park, Y. S. Kim, Chem. Commun. 2013, 49, 2783.*

[15] *S. Ohira, N. Arai, Phys. Status Solidi C 2008, 5, 3116.*

[16] *T. Oshima, T. Okuno, N. Arai, Y. Kobayashi, S. Fujita, Jpn. J. Appl. Phys. 2009, 48, 040208.*

[17] *T. Kamiya, K. Nomura, H. Hosono, Sci. Technol. Adv. Mater. 2010, 11, 044305.*

[18] *R. A. Street, Adv. Mater. 2009, 21, 2007.*

[19] *L.-X. Qian, Z.-H. Wu, Y.-Y. Zhang, P. T. Lai, X.-Z. Liu, Y.-R. Li, ACS Photonics 2017, 4, 2203.*

[20] *H. S. Bae, M. H. Yoon, J. H. Kim, S. Im, Appl. Phys. Lett. 2003, 83, 5313.*

Copyright:
DOI: 10.1002/adom.201901833;
Z. Han, H. Liang, W. Huo;
Advanced Optical Materials;

04 Multiscale and Uniform Liquid Metal Thin-Film Patterning Based on Soft Lithography for 3D Heterogeneous Integrated Soft Microsystems: Additive Stamping and Subtractive Reverse Stamping

Min-gu Kim, Choongsoon Kim, Hommood Alrowais et al.

ABSTRACT

The use of intrinsically soft conductors, such as liquid eutectic gallium–indium alloy (EGaIn), has enabled the fabrication of bioinspired soft electronics. The fabrication of EGaIn thin films with high resolution and size scalability is one of the primary technical hurdles. Soft lithography using wetting/nonwetting surface modifications and 3D heterogeneous integration can address these challenges. This study demonstrates multiscale EGaIn thin-film patterning by utilizing additive stamping for large-scale (mm–cm) soft electronics and subtractive reverse stamping for microscale (μm–mm) soft electronics. These structures can be integrated to fabricate several functional soft microsystems.

INTRODUCTION

Bioinspired soft functional material synthesis [1,2] and manufacturing technology [3,4] for soft electronics has applications ranging from entertainment to healthcare. [5,6] Unlike conventional solid-state electronics, soft electronics are lightweight, stretchable, reconfigurable, and biocompatible for skin-mountable and wearable sensors. [7,8] Flexibility and stretchability are achieved by using either 3D solid metal patterns [9,10] or elastic polymer matrices with embedded conductive nanomaterials. [11,12]

An alternative approach to realize soft microsystems is to use intrinsically soft conductors, e.g., liquid eutectic gallium–indium alloy (EGaIn). EGaIn-based soft electronics are nontoxic, mechanically stable, and highly stretchable. Also, the low melting temperature (< 15 °C (59 °F)) and negligible vapor pressure facilitate room-tempera-

ture and ambient pressure manufacturing. [13–15] Moreover, thanks to the formation of a thin oxide layer on the EGaIn surface, [16,17] the formed structures maintain their mechanical shapes on a soft elastomeric substrate, such as poly(dimethylsiloxane) (PDMS).

A broad range of patterning methods based on lithography-enabled stamping and stencil printing, injection, as well as additive and subtractive direct write/patterning processes have been implemented for EGaIn microsystems. [18–24] Limitations of lithography-defined stencils are the relatively low resolution, rough EGaIn surface, and excessive EGaIn loss during the stencil lift-off process. Subtractive direct patterning techniques using laser ablation [25,26] or electrochemical reduction [27,28] enable an inexpensive and facile approach to pattern fine EGaIn lines, but the serial process makes EGaIn removal slow in the case of patterning small EGaIn features on large substrates. Further, manually spreading EGaIn using a roller results in rough surfaces with holes in the EGaIn film. [18] Direct write and injection techniques address this issue, [29–32] but the resolution is limited. Microfluidic injection [33,34] and vacuum filling [35,36] provide high resolution, but the microchannels require relatively large thicknesses. Using a microtransfer deposition process based on soft lithography, [37] EGaIn features > 2 µm can be achieved, but the technology suffers from residues formed outside of the channel areas.

Soft lithography offers a simple, fast, and low-cost way to pattern multiscale EGaIn films. However, the surface oxide layer on EGaIn interferes with uniform wetting on soft elastomeric substrates. Stamp lithography is often regarded as the lowest resolution and

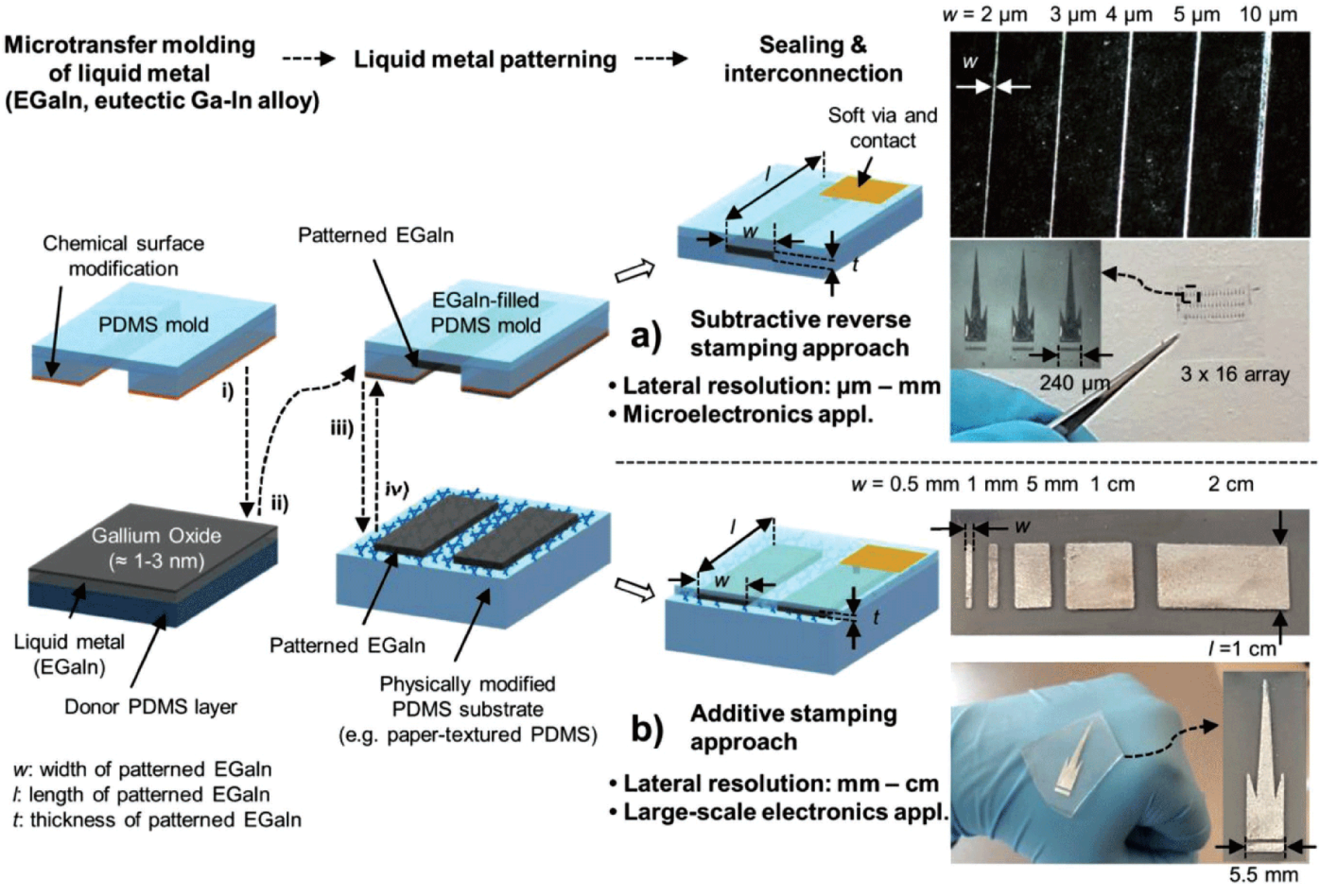

Figure 1: Schematic illustration of the multiscale and uniform EGaIn thin-film patterning process by utilizing a) subtractive reverse stamping for microscale and high-density EGaIn lines embedded in a selectively chemical-surface-modified PDMS microchannel and b) additive stamping for centimeter-scale and large-area EGaIn patterning on a physical-surface-modified PDMS substrate.

least reliable technique among the additive printing methods. [18,19,38] By utilizing chemical and physical surface modification of the elastomeric substrates, [39,40] the PDMS surfaces can be modified to have selective nonwetting or wetting properties. The nonwetting characteristics of chemically modified PDMS surfaces hinder the formation of EGaIn residue, while the uniform wetting characteristics of physically modified PDMS surfaces assist in the formation of thin and smooth films.

Recently, we demonstrated high resolution, uniform, and residue-free EGaIn patterning, ranging from single micrometer to millimeter scales, by utilizing a chemical surface modification and residue transfer process using a reverse stamping approach. [41] Building on our previous work, [41–44] this study presents multiscale and uniform EGaIn thin-film patterning by utilizing additive stamping for largescale (mm–cm) soft electronics and the subtractive reverse stamping for microscale (μm–mm) soft electronics. By combining these complementary patterning techniques using 3D heterogeneous integration, fabricated and optimized soft electronic components built with different patterning processes can be integrated to form high-density and multifunctional soft microsystems.

METHODS

Figure 1 illustrates the complementary multiscale EGaIn thin-film patterning processes based on soft lithography. The underlying liquid metal patterning processes mainly consist of three steps: 1) microtransfer molding of EGaIn, 2) EGaIn transfer using subtractive reverse stamping or additive stamping, and 3) sealing and interconnection. Chemical surface modification of the PDMS mold (for the subtractive approach) or the PDMS stamp (for the additive approach) using toluene is performed to increase the hydrophobicity. The PDMS mold/stamp is then coated by pressing onto a donor PDMS substrate coated with EGaIn.

For the subtractive approach (Figure 1a), the PDMS stamp is reverse stamped to remove EGaIn residue on the protruding surfaces to a sacrificial PDMS layer. The reverse stamping process yields fine, uniform, and thin EGaIn lines inside of the PDMS channels without residues on the surrounding protruding surfaces. Information). The subtractive approach showed size scalability from 2 μm to 1 mm – 2 mm in line width. [41]

For the additive stamping approach, a PDMS stamp wet with EGaIn is stamped onto a

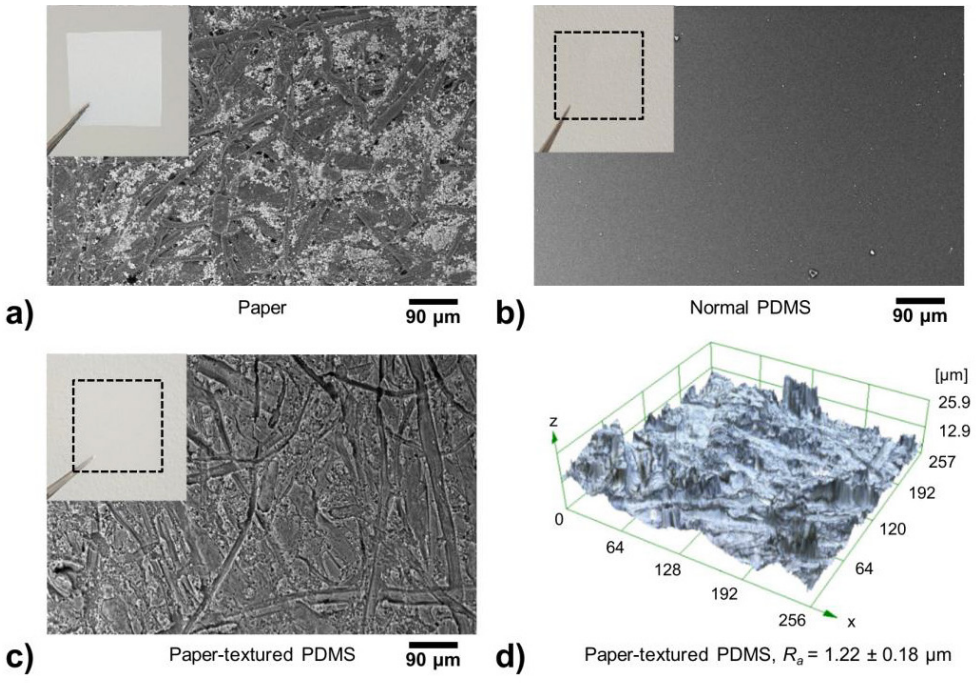

Figure 2: SEM images of a) paper, b) standard PDMS, and c) paper-textured PDMS. d) 3D laser scanning confocal microscopy image of the paper-textured PDMS surface.

paper-textured PDMS substrate (Figure 1b). The paper texture, comprised of randomly distributed micro cellulose fibers (Figure 2a), is transferred to a PDMS surface using a conventional PDMS casting method. The resulting paper-texture PDMS exhibits a surface microstructure which allows it to be wet by EGaln (Figure 2b–d). As a result, continuous EGaln films can be transferred to paper-textured PDMS with multiple stamping steps.

Surface characterizations were performed using an Olympus® LEXT™ OLS4000 3D laser scanning confocal microscope and scanning elec-

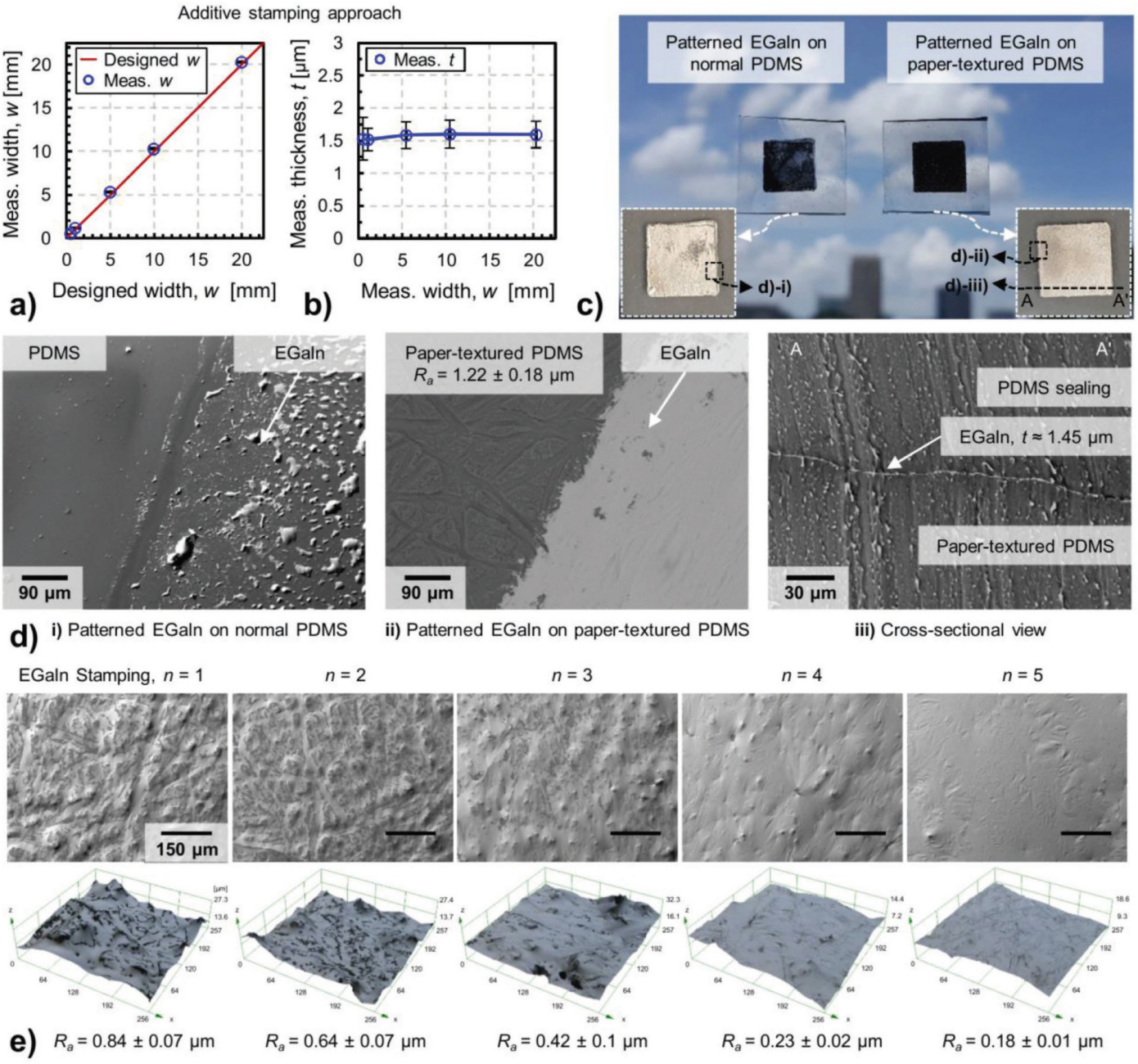

Figure 3: a) Measured EGaln width as a function of designed stamp width and b) resulting film thickness as a function of patterned EGaln width. c,d) Patterned EGaln films on standard and paper-textured PDMS surfaces and a cross-sectional view of patterned EGaln film on paper-textured PDMS after sealing with an additional PDMS layer. e) Reflection mode scanning laser confocal microscopy characterization of the EGaln thin film as a function of the number of stamping steps *(n)*.

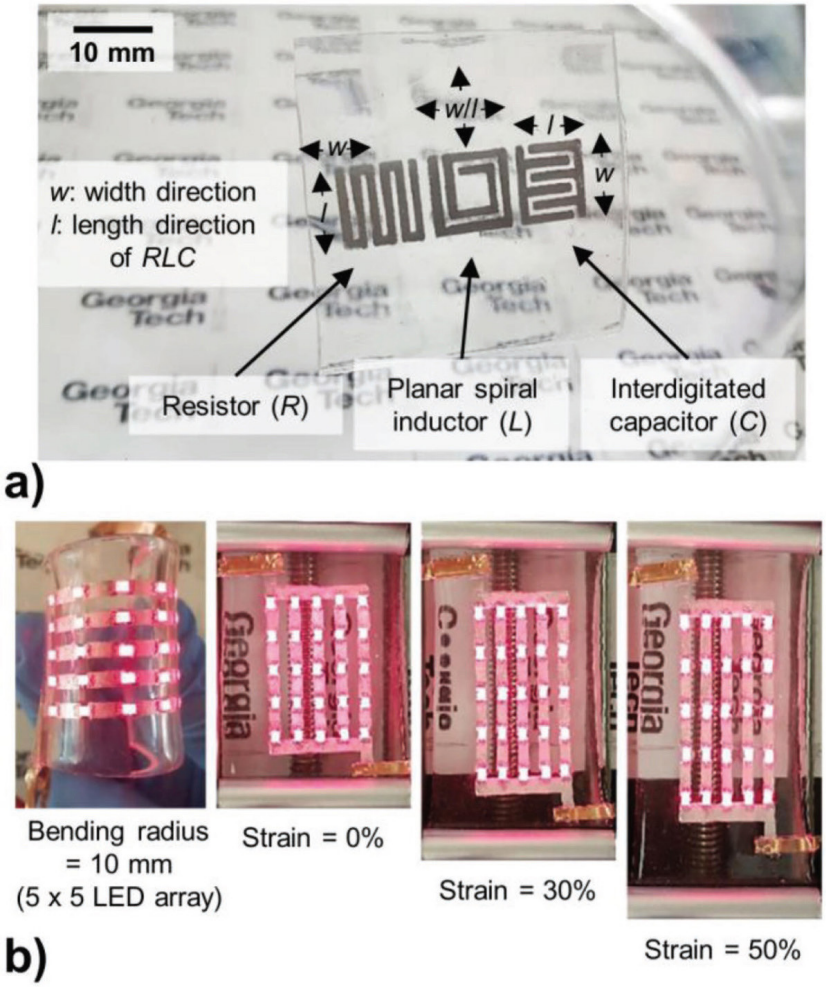

Figure 4: a) Soft, passive components fabricated using additive stamping, including a resistor, planar spiral inductor, and interdigitated capacitor. b) Soft circuit with embedded LEDs (5 × 5 array) operated under bending (r = 10 mm) and stretching (ε = 50%) deformation.

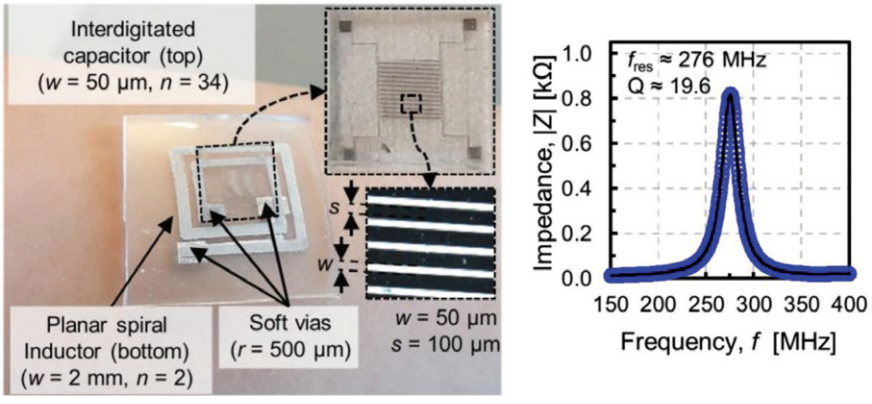

Figure 5: Demonstration of 3D heterogeneous integration and resulting performance of soft LC resonator.

tron microscopy (SEM, Hitachi S-3700N Variable Pressure SEM). Electrical characterizations of the soft, passive components, circuits, and LC resonator were performed using a multimeter (Hewlett Packard 34401A), a source meter (Keithley 2636A), and an LCR meter (Agilent 4284A). For mechanical stretching and bending characterizations, a linear motion stage and circular glass cylinders (radius: 10 mm (0.4 in.)) were prepared, respectively. Thermal characterizations of the soft heater were performed using a source meter (Keithley 2636A) to supply power, and temperature increases were recorded using an IR camera (FLIR T640).

RESULTS AND DISCUSSION

Figure 3a,b shows the measured EGaIn width as a function of the stamp width and the resulting film thickness as a function of the patterned EGaIn width, respectively. Figure 3c,d shows the non-uniform patterned EGaIn films deposited on a standard PDMS surface and a smooth uniform EGaIn film on paper-textured PDMS surface. PDMS stamps were stamped five times on paper-textured PDMS substrates to achieve smooth and uniform films. Figure 3e shows the SEM and 3D scanning laser confocal microscopy reflection mode images of stamped EGaIn, showing the evolution of the height variation with successive stamping. The additive stamping process decreases the surface roughness (Ra) with an increasing number of stamping steps, which indicates that the stamped EGaIn film is getting smoother. The random, micrometer-sized features, as characterized by scanning confocal laser microscopy in reflection mode, on the paper-textured PDMS surface (Figure 2b) were partially wetted during the initial one to two stamping steps, ultimately filling the grooved areas with EGaIn. After stamping five times, the surface structures of the paper-textured PDMS were entirely covered with EGaIn, showing a uniform and smooth EGaIn thin film.

Using the additive stamping process, soft, passive components and circuits were fabricated, and their electrical and mechanical characteristics were investigated. Figure 4a shows a soft resistor, planar spiral inductor, and interdigitated capacitor, all having a 1 mm (0.04 in.) line width and 1 mm (0.04 in.) line spacing. Figure 4b shows a simple circuit comprised of a 5 × 5 array of light-emitting diodes (LED). A constant current was applied to the LED array, which was subjected to bending (bending radius, r = 10 mm (0.4 in.)) and stretching

(strain, ε) deformation. The soft circuit withstood the bending and strain deformations (up to ε = 50%) while maintaining its functionality.

By combining the proposed multiscale EGaIn thin-film patterning techniques via 3D heterogeneous integration, more complex soft microsystems were fabricated. Three different soft functional microsystems were fabricated: i) a soft inductor-capacitor (LC) resonator, ii) a fingertip-mountable, soft oximeter, and iii) soft heaters with localized or distributed heating. Figure 5 shows the LC resonator. The interdigitated capacitor was fabricated using subtractive reverse stamping, and its areal capacitance was 13.2 pF cm^{-2}, which is roughly nine times higher than what would be achievable with additive stamping. The planar coil

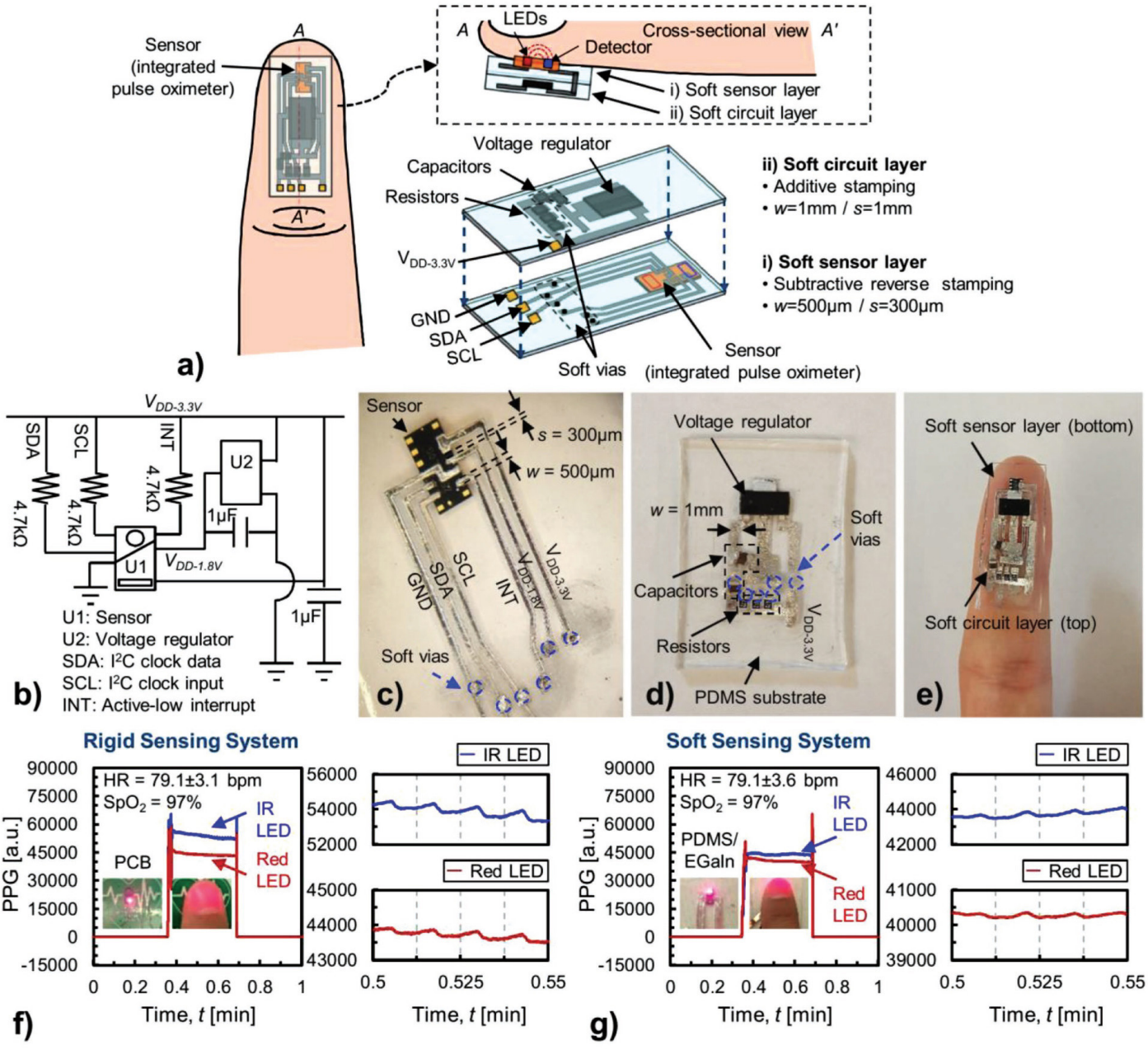

Figure 6: a) Demonstration of a fingertip-mountable soft pulse oximeter. b) Circuit diagram; fabrication and electric component integration of c) soft sensor layer and d) soft circuit layer. e) 3D-integrated microsystem mounted on a fingertip. Measured PPG waveforms of IR LED and red LED using f) PCB-based rigid sensing system and g) PDMS/EGaIn-based soft sensing system.

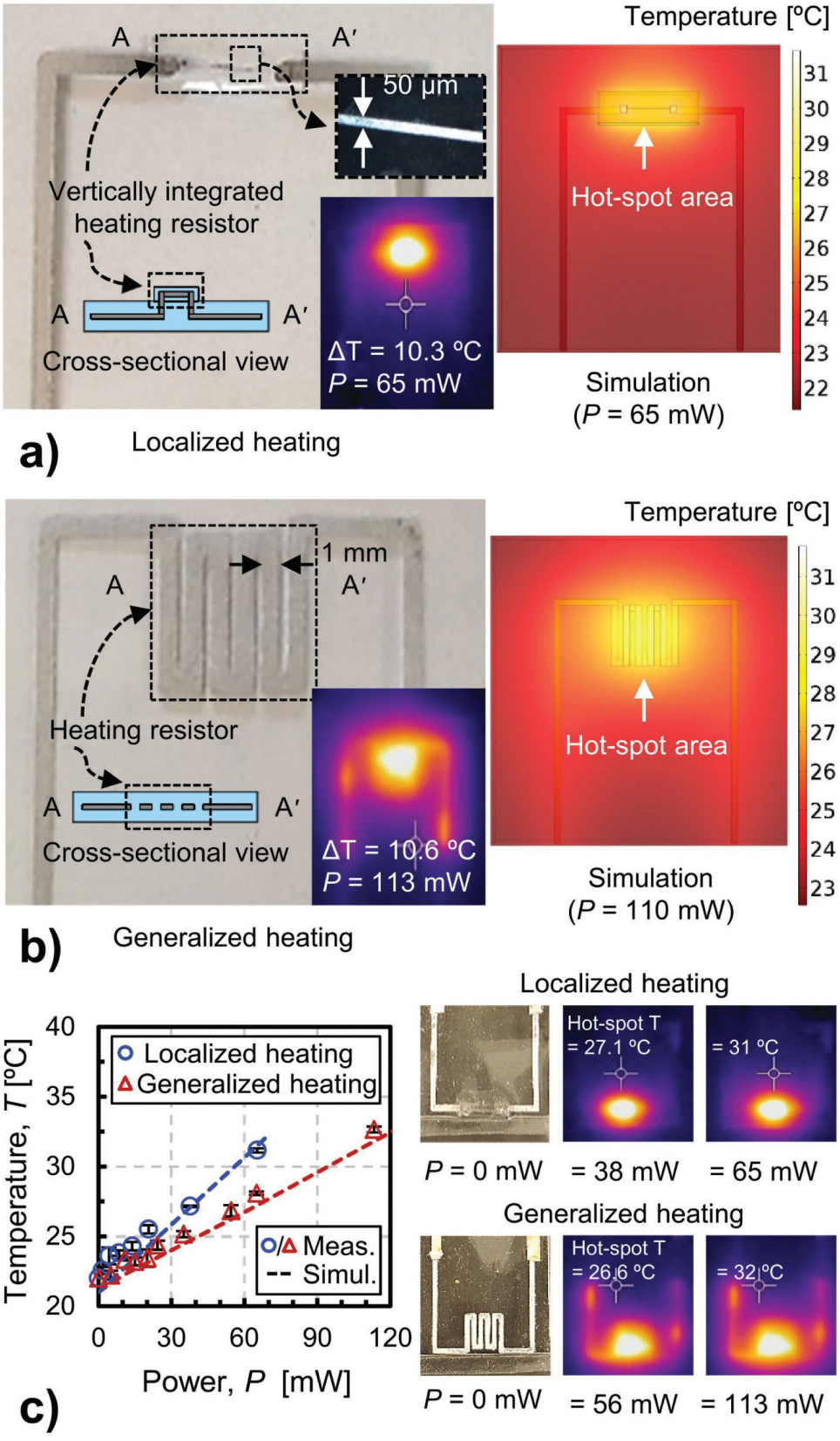

Figure 7: Demonstration of soft heaters for a) localized and b) distributed heating applications. c) Simulated and measured hot-spot temperature as a function of applied heating power.

inductor, as well as the readout coil, were fabricated using additive stamping. After 3D integration of the LC components using liquid-metal filled vias, the soft microsystem was wirelessly interrogated using a readout coil to collect the resonance frequency. The measured resonance frequency was 276 MHz, which also agreed well with the calculated value, and the Q factor was ≈20 (Figure 5b).

A fingertip-mountable, soft, and 3D-integrated biological sensor, comprised of a soft sensing layer with a commercial pulse oximeter and a soft interfacing circuit layer, is demonstrated for noninvasive and real-time heart rate (HR) and blood oxygen monitoring (Figure 6a). This soft sensor layer is fabricated using subtractive reverse stamping to connect the integrated pulse oximeter (MAX30100, Maxim Integrated Products Inc.), while additive stamping is utilized to fabricate the soft printed circuit board for the interfacing circuit (Figure 6b–d). These soft sensor and circuit layers are then vertically interconnected through soft vias (Figure 6e). The photoplethysmogram (PPG) waveforms using an IR LED and a red LED, and the extracted HR and saturation of peripheral oxygen (SpO_2) using the PDMS/EGaIn-based soft sensing system are shown in Figure 6f,g. The results were comparable to a rigid PCB-based sensing system.

Finally, soft heaters based on EGaIn thin-film resistors are demonstrated for localized and distributed heating applications. For the localized heating applications (Figure 7a), a 50 μm wide heating resistor fabricated using subtractive reverse stamping and was vertically integrated on a soft circuit. For large area heating applications (Figure 7b), a 1 mm (0.04 in.) wide serpentine heating resistor was fabricated using additive stamping. Figure 7c shows the measured and simulated hot-spot temperature as a function of the applied power. To reach a temperature increase of $\Delta T \approx 10$ °C (50 °F), the vertically integrated microheater requires 65 mW, while the serpentine-shaped heater heats a larger area but requires 113 mW. Compared to other heaters, [45–47] the fabricated soft heaters using thin-film resistors showed 8 times higher heating efficiency. In addition to efficient heating, the soft heater provides flexibility and stretchability for wearable and skin mountable electronics applications.

CONCLUSIONS

This study reports the multiscale and uniform, thin-film patterning of EGaIn using soft lithography by utilizing subtractive reverse stamping for high-density microscale patterns and additive stamping for centimeter-scale patterns. Considering the size scalability of the thin-film patterning and the possibility to heterogeneously integrate structures fabricated with either technique, soft electronic components can be fabricated and integrated to form soft and flexible multifunctional microelectronics.

REFERENCES

[1] *A. Thomas, Angew. Chem., Int. Ed. 2010, 49, 8328.*

[2] *X. Chen, H. Fuchs, Soft Matter Nanotechnology, Wiley-VCH, Weinheim 2015.*

[3] *R. L. Truby, J. A. Lewis, Nature 2016, 540, 371.*

[4] *C. S. O'Bryan, T. Bhattacharjee, S. R. Niemi, S. Balachandar, N. Baldwin, S. T. Ellison, C. R. Taylor, W. G. Sawyer, T. E. Angelini, MRS Bull. 2017, 42, 571.*

[5] *A. M. Hussain, M. M. Hussain, Adv. Mater. 2016, 28, 4219.*

[6] *A. Chortos, Z. Bao, Mater. Today 2014, 17, 321.*

[7] *J. A. Rogers, R. Ghaffari, D.-H. Kim, Stretchable Bioelectronics for Medical Device and Systems, Springer, Switzerland 2016.*

[8] *T. Someya, Stretchable Electronics, Wiley-VCH, Weinheim 2012.*

[9] *S. Xu, Y. Zhang, L. Jia, K. E. Mathewson, K.-I. Jang, J. Kim, H. Fu, X. Huang, P. Chava, R. Wang, S. Bhole, L. Wang, Y. J. Na, Y. Guan, M. Flavin, Z. Han, Y. Huang, J. A. Rogers, Science 2014, 344, 70.*

[10] *S. Xu, Z. Yan, K.-I. Jang, W. Huang, H. Fu, J. Kim, Z. Wei, M. Flavin, J. McCracken, R. Wang, A. Badea, Y. Liu, D. Xiao, G. Zhou, J. Lee, H. U. Chung, H. Cheng, W. Ren, A. Banks, X. Li, U. Paik, R. G. Nuzzo, Y. Huang, Y. Zhang, J. A. Rogers, Science 2015, 347, 154.*

[11] *K. Chen, W. Gao, S. Emaminejad, D. Kiriya, H. Ota, H. Y. Y. Nyein, K. Takei, A. Javey, Adv. Mater. 2016, 28, 4397.*

[12] *M. Segev-Bar, H. Haick, ACS Nano 2013, 7, 8366.*

[13] *M. D. Dickey, R. C. Chiechi, R. J. Larsen, E. A. Weiss, D. A. Weitz, G. M. Whitesides, Adv. Funct. Mater. 2008, 18, 1097.*

[14] *N. Kazem, T. Hellebrekers, C. Majidi, Adv. Mater. 2017, 29, 1605985.*

[15] *K. Khoshmanesh, S.-Y. Tang, J. Y. Zhu, S. Schaefer, A. Mitchell, K. Kalantar-zadeh, M. D. Dickey, Lab Chip 2017, 17, 974.*

[16] *M. D. Dickey, ACS Appl. Mater. Interfaces 2014, 6, 1836.*

[17] *R. C. Chiechi, E. A. Weiss, M. D. Dickey, G. M. Whitesides, Angew. Chem. 2008, 120, 148.*

[18] *I. D. Joshipura, H. R. Ayers, C. Majidi, M. D. Dickey, J. Mater. Chem. C 2015, 3, 3834.*

[19] *M. A. H. Khondoker, D. Sameoto, Smart Mater. Struct. 2016, 25, 093001.*

[20] *M. D. Dickey, Adv. Mater. 2017, 29, 1606425.*

[21] *S. H. Jeong, A. Hagnab, K. Hjort, M. Jobs, J. Sundqvist, Z. Wu, Lab Chip 2012, 12, 4657.*

[22] *N. Lazarus, S. S. Bedair, I. M. Kiezewski, ACS Appl. Mater. Interfaces 2017, 9, 1178.*

[23] *C. W. Park, Y. G. Moon, H. Seong, S. W. Jung, J.-Y. Oh, B. S. Na, N.-M. Park, S. S. Lee, S. G. Im, J. B. Koo, ACS Appl. Mater. Interfaces 2016, 8, 15459.*

[24] *Q. Zhang, Y. Gao, J. Liu, Appl. Phys. A 2014, 116, 1091.*

[25] *T. Lu, L. Finkenauer, J. Wissman, C. Majidi, Adv. Funct. Mater. 2014, 24, 3551.*

[26] *T. Lu, E. J. Markvcika, Y. Jin, C. Majidi, ACS Appl. Mater. Interfaces 2017, 9, 22055.*

[27] *M. R. Khan, C. B. Eaker, E. F. Bowden, M. D. Dickey, Proc. Natl. Acad. Sci. USA 2014, 11, 14047.*

[28] *M. R. Khan, J. Bell, M. D. Dickey, Adv. Mater. Interfaces 2016, 3, 1600546.*

[29] *J. W. Boley, E. L. White, G. T.-C. Chiu, R. K. Kramer, Adv. Mater. 2010, 22, 2749.*

[30] *C. Ladd, J.-H. So, J. Muth, M. D. Dickey, Adv. Mater. 2013, 25, 5081.*

[31] *Y. Zheng, Z. He, Y. Gao, J. Liu, Sci. Rep. 2013, 3, 1786.*

[32] *Q. Wang, Y. Yu, J. Yang, J. Liu, Adv. Mater. 2015, 27, 7109.*

[33] *Y.-L. Park, B.-P. Chen, R. J. Wood, IEEE Sens. J. 2012, 12, 2711.*

[34] *M. Kubo, X. Li, C. Kim, M. Hashimot, B. J. Wiley, D. Ham, G. M. Whitesides, Adv. Funct. Mater. 2014, 24, 3501.*

[35] *B. L. Cumby, G. J. Hayes, M. D. Dickey, R. S. Justice, C. E. Tabor, J. C. Heikenfeld, Appl. Phys. Lett. 2012, 101, 174102.*

[36] *Y. Lin, O. Gordon, M. R. Khan, N. Vasquez, J. Genzer, M. D. Dickey, Lab Chip 2017, 17, 3043.*

[37] *B. A. Gozen, A. Tabatabai, O. B. Ozdoganlar, C. Majidi, Adv. Mater. 2014, 26, 5211.*

[38] *A. Tabatabai, A. Fassler, C. Usiak, C. Majidi, Langmuir 2013, 29, 6194.*

[39] *D. Kim, Y. Lee, D.-W. Lee, W. Choi, K. Yoo, J.-B. Lee, Sens. Actuators, B 2015, 207, 199.*

[40] *G. Li, M. Parmar, D.-W. Lee, Lab Chip 2015, 15, 766.*

[41] *M. Kim, H. Alrowais, S. Pavlidis, O. Brand, Adv. Funct. Mater. 2017, 27, 1604466.*

[42] *M. Kim, H. Alrowais, C. Kim, P. Yeon, M. Ghovanloo, O. Brand, Lab Chip 2017, 17, 2323.*

[43] *M. Kim, H. Alrowais, O. Brand, presented at IEEE Int. Conf. Microelectro-mech. Syst., Las Vegas, January 2017.*

[44] *M. Kim, H. Alrowais, O. Brand, Adv. Electron. Mater. 2018, 4, 1700434.*

[45] *J. Je, J. Lee, J. Micro-mech. Syst. 2014, 23, 1156.*

[46] *H. Ota, S. Emaminejad, Y. Gao, A. Zhao, E. Wu, S. Challa, K. Chen, H. M. Fahad, A. K. Jha, D. Kiriya, W. Gao, H. Shiraki, K. Morioka, A. R. Ferguson, K. E. Healy, R. W. Davis, A. Javey, Adv. Mater. Technol. 2016, 1, 1600013.*

[47] *N. Lazarus, B. Hanrahan, Adv. Mater. Technol. 2016, 1, 1600130.*

Copyright:
DOI: 10.1002/admt.201800061;
M.-g. Kim, C. Kim, H. Alrowais, O. Brand;
Advanced Materials Technologies;

Scientific Publishing

WHY IS A COVER LETTER to the editor so important? Which information should be included into the title and abstract? These and more questions will be answered in this section.

5 tips for writing better science papers

1

Don't underestimate the importance of your cover letter

A good cover letter explains to the editor the critical question your research addresses, how you have answered this question, and why it is of significance to the wider community.

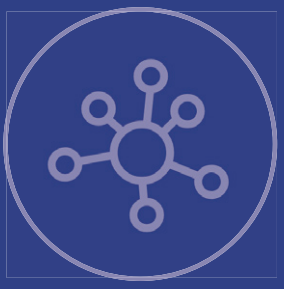

2

Keep the title simple: be consistent, not too technical, and concise

It's important to grab the attention of your editor/reviewer/reader right away and give them an idea of why your paper is a scientific breakthrough. The title also plays into search engine optimization for your article, so think of which search terms you would use when searching for your paper, and try to incorporate those keywords into your title.

4

Introduce your research with its importance

The reader needs to know the background to your research and, most importantly, why your research is important in this context. What critical questions does your research address? Why should the reader be interested?

3

Don’t cram the abstract with details

What you want is to grab the reader’s attention with the first statement, add a few of the most important details, then leave them with the overall message of the manuscript in the last sentence.

5

You might be tempted to share all your war stories… but don’t

When reporting results, keep your focus and make your R&D concise but informative.

Scientific Publishing: Getting Started

THE START of a new research project or a thesis can be an exciting experience, with all the ideas to be realized ahead. It is tempting to just begin with the practical work and think about how to publish it later; however, there are good reasons (outlined below) to plan the publication of your manuscript at the very beginning of your project:

1. You will save time

Before and during the experimental work, a thorough literature research is essential. Identify the most relevant publications for your own projects from the beginning on to use them for the introduction of your article or communication.

2. You will stay focused

If you use the method described below, you will be able to use your project's outline as orientation to maintain emphasis on the key questions you meant to target.

3. You will read research articles with different eyes

In composing a research project, other scientific articles can have two uses: as well as their content it is useful to focus on their structure, the use of language and relevant keywords. What makes a good scientific text? You will be more aware of all that when keeping your own manuscript in mind.

4. You will avoid the "fear of the blank page"

The beginning of the writing process is probably the hardest part. If you already prepared the structure of your manuscript, collected ideas and references for the introduction, phrased the key finding of your study and wrote the experimental section while conducting the research, you will have a much easier start.

WHEN IS THE BEST MOMENT TO START THE WRITING PROCESS?

According to the essay "Whitesides' Group: Writing a Paper'", by Prof. George M. Whitesides, it is useful to work with an outline to plan and conduct both your research and the corresponding paper from the project's beginning. To fulfill this function, an outline is structured like a research article – with an introduction, the results and discussion, and conclusions – and will be updated throughout the course of the project. As it contains the main questions you want to answer throughout your research, you will be able to use the outline as a tool to continuously analyze the progress and the focus of your work. In a "brainstorming" session, you can create an outline by writing down all your ideas, questions and hypotheses in any order on an empty piece of paper. Afterwards, you transfer all to another piece of paper using the structure described below.

STRUCTURE AND CONTENTS OF AN OUTLINE

"If you clearly understand the purpose and form of a paper, it can be immensely useful to you in organizing and conducting your research." For Whiteside, the purpose of a paper is not only to serve as an archive, but also as a tool for planning and conducting research. Thus, he recommends creating an outline that is already structured like a scientific article:

- ### Title

At the beginning this will necessarily be a working title; you should try to formulate the key goal of your research here (we will provide you with tips for creating an article's title in a later edition).

- ### Abstract

You will leave this section empty at the beginning; you will learn more about writing an abstract later.

- ### Introduction

At the beginning, you use this part of the outline to define the objective of your work and why it is important; based on the literature research you conducted beforehand, you formulate the background and fundamentals of your research; whenever you find a relevant study, you should add it and its key findings to this section.

- ### Results and Discussion

In here, you should add the major points you plan to target in your project. This could look as follows:

Synthesis of the monomers
Polymerization reactions
Characterization methods
Applications

In the course of conducting your research, you add all your results into the respective parts of this section. You will most likely find out that some of the original plans need to be adapted due to unexpected findings; use the results and discussions section as a tool to constantly summarize, analyze and, if necessary, update your key goals of your project.

- ### Conclusions

For the outline, you can condense your conclusions to short phrases; compare them to the key objectives you framed in the introduction – do they match or need reformulation?

- ### Experimental

You will save a lot of time at the end of your thesis or project if you ensure you write down all experimental findings from the beginning on.

Herein, we outlined one of many ways to successfully conduct your research and the writing process. In the next editions of our "Tips on Scientific Publishing", we will give a more detailed look at the different sections of a scientific article.

We highly recommend reading the short essay by Prof. Whiteside (freely available):

Whitesides, G. (2004), Whitesides' Group: Writing a Paper. Adv. Mater., 16: 1375-1377. doi:10.1002/adma.200400767